arXiv:1606.00390v1 [physics.optics] 24 Nov 2015

Modal formulation for diffraction by absorbing photonic crystal slabs

Kokou B. Dossou[1,*], Lindsay C. Botten[1], Ara A. Asatryan[1], Björn C.P. Sturmberg[2], Michael A. Byrne[1], Christopher G. Poulton[1], Ross C. McPhedran[2], and C. Martijn de Sterke[2]

[1] *CUDOS, University of Technology, Sydney, N.S.W. 2007, Australia*

[2] *CUDOS and IPOS, School of Physics, University of Sydney, NSW 2006, Australia*

[*] *Corresponding author: Kokou.Dossou@uts.edu.au*

A finite element-based modal formulation of diffraction of a plane wave by an absorbing photonic crystal slab of arbitrary geometry is developed for photovoltaic applications. The semi-analytic approach allows efficient and accurate calculation of the absorption of an array with a complex unit cell. This approach gives direct physical insight into the absorption mechanism in such structures, which can be used to enhance the absorption. The verification and validation of this approach is applied to a silicon nanowire array and the efficiency and accuracy of the method is demonstrated. The method is ideally suited to studying the manner in which spectral properties (e.g., absorption) vary with the thickness of the array, and we demonstrate this with efficient calculations which can identify an optimal geometry. © 2016 Optical Society of America

OCIS codes: 050.1960, 290.0290, 350.6050, 160.5293.

1. Introduction

Photonic crystals, which consist of a periodically arranged lattice of dielectric scatterers, have attracted substantial research interest over the past decade [1]. Most commonly these structures are used to trap, guide, and otherwise manipulate pulses of light, and have led to a variety of important applications in modern nanophotonics, including extremely high-Q electromagnetic cavities [2] and slow-light propagation of electromagnetic pulses [3]. However, a new and increasingly important application of photonic crystal structures is in the field of photovoltaics. It has long been known that structured materials can be used to achieve

photovoltaic conversion efficiency beyond the Yablonovitch limit [4,5], and indeed researchers have recently proposed photonic crystals [6, 7] and arrays of dielectric nanowires [8, 9] as inexpensive ways to create highly efficient absorbers. Recent research in this area has been driven by advances in nanostructure fabrication [10] concurrent with increased investment in renewable energy technology (for the latest developments see [11]).

One aspect in which the use of photonic crystals in photovoltaics differs markedly from their employment in optical nanophotonics is the important role played by material absorption. For most nanophotonic applications absorption is an undesirable effect which must in general be minimized and can in many cases be neglected. This is in stark contrast to photovoltaics, in which the main aim is to exploit the properties of the structure to increase the overall absorption efficiency.

Modeling of absorbing photonic crystals has thus far been performed using direct numerical methods such as the Finite-Difference Time-Domain (FDTD) method [8], the Finite Element Method (FEM) [12] or using the Transfer Matrix method [9]. Although these methods have produced valuable information about the absorption properties of such structures they do not allow us to gain direct physical insight into the mechanism of the absorption within them. Furthermore, these calculations require substantial computational time and resources.

Here we present a rigorous modal formulation of the scattering and absorption of a plane wave by an array of absorbing nanowires, or, correspondingly, an absorbing photonic crystal slab (Fig. 1). The approach is a generalization of diffraction by capacitive grids formulated initially in Refs [13, 14] for perfectly conducting cylinders. In contrast to conventional photonic crystal calculations the material absorption is taken into account rigorously, using measured values for the real and the imaginary parts of the refractive indices of the materials comprising the array. Our formulation can be applied to array elements of arbitrary composition and cross-section. The semi-analytical nature of this modal approach results in a method which is quick, accurate, and gives extensive physical insight into the importance of the various absorption and scattering mechanisms involved in these structures.

The method is based on an expansion in terms of the fundamental eigenmodes of the structure in each different region. Within the photonic crystal slab the fields are expanded in terms of Bloch modes, while the fields in free space above and below the slab are expanded in a basis of plane waves. These expansions are then matched using the continuity of the tangential components of the fields at the top and the bottom interfaces of the slab to compute Fresnel interface reflection and transmission matrices.

An important aspect of this approach is that the set of Bloch modes must form a complete basis. This is not a trivial matter, as even for structures consisting of lossless materials the eigenvalue problem for the Bloch modes is not formally Hermitian. However, it is well known from the classical treatment of non-Hermitian eigenvalue problems [15, p. 884] that a

complete basis may be obtained by including the Bloch modes of the adjoint problem. Here, we use the FEM to compute both the Bloch modes and the adjoint Bloch modes. Because the mode computation may be carried out in two dimensions (2D) like waveguide mode calculations, this routine is highly efficient. We note that a previous study [16], undertaken using a different method, failed to locate some of the modes, as is demonstrated in Sec. 3.A; we emphasis that the algorithm presented here is capable of generating a complete set of modes. In addition the FEM allows us to compute Bloch modes for arbitrary materials and cross sections.

We note that this approach differs from earlier formulations [13, 14] in which the photonic crystal had to consist of an array of cylinders with a circular cross-section. With the modes identified, the transmission through, and reflection from, the slab can be computed using a generalization of Fresnel reflection and transmission matrices, and the absorption is found using an energy conservation relation.

The organization of the paper is as follows. The theoretical foundation of the method is given in Sec. 2 while the numerical verification, validation and characterization of the absorption properties of a particular silicon nanowire array occurs in Sec. 3. The details of the mode orthogonality, normalization, completeness as well as energy and reciprocity relations are given in the appendices.

2. Theoretical description

As mentioned in Sec. 1, we separate the solution of the diffraction problem into three steps, one involving the consideration of the scattering of plane waves at the top interface and the introduction of the Fresnel reflection and the transmission matrices for a top interface (Fig. 1). Next we introduce the Fresnel reflection and transmission matrices for the bottom interface by considering the reflection of the waveguide modes of the semi-infinite array of cylinders at the bottom interface. Then the total reflection and transmission through the slab can be calculated using a Fabry-Perot style of analysis. The approach is based on the calculation of the Bloch modes and adjoint Bloch modes of an infinite array of cylinders. Before doing so however, we first provide the field's plane wave expansions above and below the photonic crystal slab.

2.A. Plane wave expansion

In a uniform media such as free space, all components of the electromagnetic field of a plane wave must satisfy the Helmholtz equation

$$\nabla^2 \boldsymbol{E} + k^2 \boldsymbol{E} = 0, \tag{1}$$

where $k = 2\pi/\lambda$ is the free space wavenumber. Here we consider the diffraction of a plane wave on a periodic square array of cylinders with finite length (see Fig. 1). In such a structure,

the fields have a quasi-periodicity imposed by the incident plane wave field $\exp(i(\alpha_0 x+\beta_0 y-\gamma_{00}z))$, where $\gamma_{00}=\sqrt{k^2-\alpha_0^2-\beta_0^2}$. That is,

$$\boldsymbol{E}(\boldsymbol{r}+\boldsymbol{R})=\boldsymbol{E}(\boldsymbol{r})e^{i\boldsymbol{k}_0\cdot\boldsymbol{R}}, \tag{2}$$

where $\boldsymbol{k}_0=(\alpha_0,\beta_0)$ and $\boldsymbol{R}=(s_1 d, s_2 d)$ is a lattice vector, where s_1 and s_2 are integers. All plane waves of the form $\exp(i(\alpha x+\beta y\pm\gamma z))=\exp(i(\boldsymbol{k}_\perp\cdot\boldsymbol{r}))\exp(\pm i\gamma z)$, must satisfy the Bloch condition Eq. (2) and so $e^{i\boldsymbol{k}_\perp\cdot\boldsymbol{R}_s}=e^{i\boldsymbol{k}_0\cdot\boldsymbol{R}_s}$. Hence $(\boldsymbol{k}_\perp-\boldsymbol{k}_0)\cdot\boldsymbol{R}_s=2\pi m$, where m is an integer. It follows then that the coefficients α and β are discretized as follows

$$\alpha_p = \alpha_0+p\,\frac{2\pi}{d}\,, \tag{3}$$

$$\beta_q = \beta_0+q\,\frac{2\pi}{d} \tag{4}$$

and form the well known diffraction grating orders.

We split the electromagnetic field into its transverse electric TE and the transverse magnetic TM components (see, for example, Ref. [17]) . For the transverse electric mode, the electric field is perpendicular to the plane of incidence, while for the transverse magnetic mode the magnetic field vector is perpendicular to the plane of incidence—with the plane of incidence being defined by the z-axis and the plane wave propagation direction given by the vector $\boldsymbol{k}_0$. These TE and TM resolutes are given by

$$\begin{aligned}\boldsymbol{R}_s^E(x,y) &= -\frac{i}{Q_s}\boldsymbol{e}_z\times\nabla_\perp V_s\\ &= \frac{\boldsymbol{e}_z\times\boldsymbol{Q}_s}{Q_s}V_s(x,y),\end{aligned} \tag{5}$$

$$\boldsymbol{R}_s^M(x,y) = -\frac{i}{Q_s}\nabla_\perp V_s=\frac{\boldsymbol{Q}_s}{Q_s}V_s(x,y), \tag{6}$$

$$\boldsymbol{Q}_s = (\alpha_p,\beta_q), \tag{7}$$

respectively, where $V_s(x,y)=\exp(i\,\boldsymbol{Q}_s\cdot\boldsymbol{r})$. The TE and TM plan wave modes are mutually orthogonal, and are normalized such that

$$\iint \boldsymbol{R}_p^a\cdot\overline{\boldsymbol{R}}_q^b\,dS = \delta_{ab}\delta_{pq}, \tag{8}$$

where the overline in $\overline{\boldsymbol{R}}_q^b$ denotes complex conjugation and the integration is over the unit cell.

The general form of the plane wave expansions above and below the grating (see Fig. 1) can then be written in terms of these TE and TM modes. Following the nomenclature of

Ref. [17], the plane wave expansions take the forms

$$\begin{aligned}
\boldsymbol{E}_\perp(\boldsymbol{r}) &= \sum_s \chi_s^{-1/2} \left[f_s^{E-} e^{-i\gamma_s(z-z_0)} \right. \\
&+ \left. f_s^{E+} e^{i\gamma_s(z-z_0)} \right] \boldsymbol{R}_s^E(\boldsymbol{r}) \\
&+ \chi_s^{1/2} \left[f_s^{M-} e^{-i\gamma_s(z-z_0)} \right. \\
&+ \left. f_s^{M+} e^{i\gamma_s(z-z_0)} \right] \boldsymbol{R}_s^M(\boldsymbol{r}) \qquad (9) \\
\boldsymbol{e}_z \times \boldsymbol{H}_\perp(\boldsymbol{r}) &= \sum_s \chi_s^{1/2} \left[f_s^{E-} e^{-i\gamma_s(z-z_0)} \right. \\
&- \left. f_s^{E+} e^{i\gamma_s(z-z_0)} \right] \boldsymbol{R}_s^E(\boldsymbol{r}) \\
&+ \chi_s^{-1/2} \left[f_s^{M-} e^{-i\gamma_s(z-z_0)} \right. \\
&- \left. f_s^{M+} e^{i\gamma_s(z-z_0)} \right] \boldsymbol{R}_s^M(\boldsymbol{r}) \qquad (10)
\end{aligned}$$

where $f_s^{E\pm}$ and $f_s^{M\pm}$ represent the amplitudes of transverse electric and magnetic component of the downward $(-)$ and upward $(+)$ propagating plane waves and

$$\gamma_s = \sqrt{k^2 - \alpha_p^2 - \beta_q^2}, \qquad (11)$$

where s denotes a plane wave channel represented by the pair of integers $s = (p, q) \in \mathbb{Z}^2$. In the numerical implementation it is convenient to order the plane waves in descending order of γ_s^2. In Eqs (9) and (10), χ_s is defined as

$$\chi_s = \frac{\gamma_s}{k}, \qquad (12)$$

and the factors $\chi_s^{\pm 1/2}$ are included to normalize the calculation of energy fluxes.

2.B. FEM calculation of modes and adjoint modes of cylinder arrays

The FEM presented here is a general purpose numerical method which can handle the square, hexagonal or any other array geometry. The constitutive materials of the array can be dispersive and lossy. We first introduce the eigenvalue problem and then we present a variational formulation and the corresponding FEM discretization.

2.B.1. Maxwell's equations

At a fixed frequency, the electric and magnetic fields of the electromagnetic modes satisfy Maxwell's equations

$$\nabla \times \boldsymbol{H} = -\, i\,k\,\varepsilon\,\boldsymbol{E}\,, \quad \nabla \cdot (\varepsilon\,\boldsymbol{E}) = 0\,, \qquad (13)$$

$$\nabla \times \boldsymbol{E} = \quad i\,k\,\mu\,\boldsymbol{H}\,, \quad \nabla \cdot (\mu\,\boldsymbol{H}) = 0\,, \qquad (14)$$

where ε and μ are the relative dielectric permittivity and magnetic permeability respectively. We express the time dependence in the form $e^{-i\omega t}$. The magnetic field $\boldsymbol{H}$ has been rescaled as $Z_0\boldsymbol{H} \to \boldsymbol{H}$ with $Z_0 = \sqrt{\mu_0/\varepsilon_0}$, the impedance of free space.

We now consider the electromagnetic modes of an array of cylinders of infinite length. The cylinder axes are aligned with the $z-$axis. The dielectric permittivity and magnetic permeability of the array are invariant with respect to z. From this translational invariance, we know that the Bloch modes of the array have a $z-$dependence $\exp(i\zeta z)$ and are quasi-periodic with respect to x and y. This reduces the problem of finding the modes to a unit cell Ω in the $xy-$plane (see Fig. 1).

As explained in Section 2.B.4, this modal problem for the cylinder arrays is not Hermitian and therefore the eigenmodes do not necessarily form an orthogonal set. However, by introducing the modes of the adjoint problem we can form a set of adjoint modes which have a biorthogonality property [18] with respect to the primal eigenmodes. In order to introduce the adjoint problem, we first write Maxwell's equations for conjugate material parameters $\overline{\varepsilon}(\boldsymbol{r})$ and $\overline{\mu}(\boldsymbol{r})$:

$$\nabla \times \boldsymbol{H}^{\mathrm{c}} = \; - \; i\,k\,\overline{\varepsilon}\,\boldsymbol{E}^{\mathrm{c}}\,, \quad \nabla\cdot(\overline{\varepsilon}\,\boldsymbol{E}^{\mathrm{c}}) = 0\,, \tag{15}$$

$$\nabla \times \boldsymbol{E}^{\mathrm{c}} = \quad\; i\,k\,\overline{\mu}\,\boldsymbol{H}^{\mathrm{c}}\,, \quad \nabla\cdot(\overline{\mu}\,\boldsymbol{H}^{\mathrm{c}}) = 0\,. \tag{16}$$

The fields $\boldsymbol{E}^{\mathrm{c}}$ and $\boldsymbol{H}^{\mathrm{c}}$ have the same time dependence and quasi-periodicity as $\boldsymbol{E}$ and $\boldsymbol{H}$. We define the adjoint modes as the conjugate fields $\boldsymbol{E}^{\dagger} = \overline{\boldsymbol{E}^{\mathrm{c}}}$ and $\boldsymbol{H}^{\dagger} = \overline{\boldsymbol{H}^{\mathrm{c}}}$, and they satisfy Maxwell's equations:

$$\nabla \times \boldsymbol{H}^{\dagger} = \quad\; i\,k\,\varepsilon\,\boldsymbol{E}^{\dagger}\,, \quad \nabla\cdot(\varepsilon\,\boldsymbol{E}^{\dagger}) = 0\,, \tag{17}$$

$$\nabla \times \boldsymbol{E}^{\dagger} = \; - \; i\,k\,\mu\,\boldsymbol{H}^{\dagger}\,, \quad \nabla\cdot(\mu\,\boldsymbol{H}^{\dagger}) = 0\,. \tag{18}$$

Therefore, the adjoint modes $\boldsymbol{E}^{\dagger}$ and $\boldsymbol{H}^{\dagger}$ satisfy the same wave equations as $\boldsymbol{E}$ and $\boldsymbol{H}$, but have the opposite quasi-periodicity and $e^{i\,\omega\,t}$ time dependence.

2.B.2. Variational formulation of the eigenvalue problem

Let Ω denote a unit cell of the periodic lattice. Within the array, a Bloch mode is a nonzero solution of the vectorial wave equation

$$\nabla \times (\mu^{-1}\nabla \times \boldsymbol{E}) - k^2\varepsilon\boldsymbol{E} = 0, \text{ on the domain } \Omega, \tag{19}$$

which is quasi-periodic in the transverse plane with respect to the wave vector $\boldsymbol{k}_{\perp}$, and has exponential z dependence, with the propagation constant ζ, i.e.

$$\boldsymbol{E}(x,y,z) = \boldsymbol{E}(x,y)\,e^{i\,\zeta\,z}. \tag{20}$$

The longitudinal and transverse components of the electric field $\boldsymbol{E}$ are respectively E_z and $\boldsymbol{E}_\perp = [E_x, E_y]^T$. At the edges of the unit cell, the tangential component $\boldsymbol{E}_\perp \cdot \vec{\tau}$ ($\vec{\tau}$ denotes a unit tangential vector to the unit cell boundary $\partial\Omega$) and the longitudinal component E_z of a Bloch mode satisfy the boundary conditions

$$\boldsymbol{E}_\perp \cdot \vec{\tau} \text{ and } E_z \text{ are } \boldsymbol{k}_\perp\text{-quasi-periodic over } \partial\Omega. \tag{21}$$

The quasi-periodicity of the components $\boldsymbol{H}_\perp \cdot \vec{\tau}$ and H_z of the magnetic field $\boldsymbol{H}$ associated with $\boldsymbol{E}$ is enforced as a "natural boundary condition" of the FEM.

Taking the exponential z dependence into account by substituting (20) into (19), one is led to the coupled partial differential equations

$$\begin{cases} \vec{\nabla}_\perp \times (\mu^{-1}(\nabla_\perp \times \boldsymbol{E}_\perp)) - i\,\zeta\mu^{-1}\nabla_\perp E_z \\ \qquad\qquad +(\zeta^2\mu^{-1} - k^2\varepsilon)\boldsymbol{E}_\perp = 0, \\ -i\,\zeta\nabla_\perp\cdot(\mu^{-1}\boldsymbol{E}_\perp) - \nabla_\perp\cdot(\mu^{-1}\nabla_\perp E_z) - k^2\varepsilon E_z = 0 \end{cases} \tag{22}$$

where the operators $\nabla_\perp E_z$ and $\nabla_\perp \cdot \boldsymbol{E}_\perp$ are the gradient and the divergence with respect to the transverse variables x and y; the transverse curl operators are defined as

$$\vec{\nabla}_\perp \times \boldsymbol{e}_z F_z = \begin{bmatrix} \frac{\partial F_z}{\partial y} \\ -\frac{\partial F_z}{\partial x} \end{bmatrix}, \tag{23}$$

$$\nabla_\perp \times \boldsymbol{F}_\perp = \left(\frac{\partial F_y}{\partial x} - \frac{\partial F_x}{\partial y}\right)\boldsymbol{e}_z. \tag{24}$$

Problem (22) is a nonlinear eigenproblem with respect to the unknown ζ since it involves both ζ and ζ^2. For $\zeta \neq 0$, the substitution

$$E_z = -i\,\zeta\hat{E}_z \tag{25}$$

leads to a generalized eigenvalue problem involving only ζ^2

$$\begin{cases} \vec{\nabla}_\perp \times (\mu^{-1}(\nabla_\perp \times \boldsymbol{E}_\perp)) - k^2\varepsilon\boldsymbol{E}_\perp \\ \qquad\qquad = \zeta^2(\mu^{-1}\nabla_\perp\hat{E}_z - \mu^{-1}\boldsymbol{E}_\perp), \\ -\nabla_\perp\cdot(\mu^{-1}\boldsymbol{E}_\perp) + \nabla_\perp\cdot(\mu^{-1}\nabla_\perp\hat{E}_z) + k^2\varepsilon\hat{E}_z = 0. \end{cases} \tag{26}$$

Note that an eigenvalue $\zeta^2 \neq 0$ of Eq. (26) corresponds to a pair of propagation constants $\zeta^+ = \zeta$ and $\zeta^- = -\zeta$ which are respectively associated with a *upward propagating* (i.e., towards $z \to \infty$) wave, $\boldsymbol{E}^+ = [\boldsymbol{E}_\perp, E_z] = [\boldsymbol{E}_\perp, -i\,\zeta^+\hat{E}_z]$ (according to the scaling (25)) and a *downward propagating* wave $\boldsymbol{E}^- = [\boldsymbol{E}_\perp, E_z] = [\boldsymbol{E}_\perp, -i\,\zeta^-\hat{E}_z]$. As shown in Ref. [19], except for a countable set of frequencies, in general all eigenvalues of the problem (26) are

nonzero. We remark that, in some cases, the mathematical analysis of the eigenproblem can be simpler and more elegant if Eq. (26) is rewritten in the following form

$$\left\{\begin{array}{l} \vec{\nabla}_\perp \times (\mu^{-1}(\nabla_\perp \times \boldsymbol{E}_\perp)) - k^2\varepsilon \boldsymbol{E}_\perp \\ \qquad\qquad = \zeta^2 \left(\mu^{-1}\nabla_\perp \hat{E}_z - \mu^{-1}\boldsymbol{E}_\perp\right), \\ 0 = \zeta^2 \left(-\nabla_\perp\cdot(\mu^{-1}\boldsymbol{E}_\perp) + \nabla_\perp\cdot(\mu^{-1}\nabla_\perp \hat{E}_z) + k^2\varepsilon \hat{E}_z\right). \end{array}\right. \tag{27}$$

For instance, as is explained below (see Eqs. (40)–(42)), the differential operators on the left and right hand sides of Eq. (27) are Hermitian, in the case of lossless gratings while, for lossy gratings, the adjoint of each operator is the complex conjugate of the operator. However, all nonzero fields of the form $\boldsymbol{E} = (0, 0, \hat{E}_z)$ become eigenmodes (although most are non-physical) of Eq. (27) associated with the zero eigenvalue. In order to avoid the unnecessary calculations of these non-physical modes, we have used a numerical implementation based on Eq. (26).

We now explain our convention used in the modal classification. Taking into account the exponential z dependence $e^{i\,\zeta\, z}$, if $\mathrm{Re}\,\zeta^2 > 0$ and $\mathrm{Im}\,\zeta^2 = 0$ (propagating mode) the upward travelling wave $\boldsymbol{E}^+$ corresponds to the positive square root of ζ^2 , i.e., $\zeta^+ > 0$; otherwise if $\mathrm{Re}\,\zeta^2 < 0$ or $\mathrm{Im}\,\zeta^2 \neq 0$ (evanescent mode) the upward travelling wave $\boldsymbol{E}^+$ corresponds to the mode such that $|e^{i\,\zeta\, z}|$ decreases as z increases, i.e., ζ^+ is the complex square root of ζ^2 such that $\mathrm{Im}\,\zeta^+ > 0$.

In order to obtain the variational formulation corresponding to the problem Eqs. (26) and (21) we introduce the following functional spaces

$$\mathcal{V} = \left\{\begin{array}{l} F_z \in L^2(\Omega) \mid \nabla_\perp F_z \in L^2(\Omega); \\ \quad F_z \text{ is } \boldsymbol{k}_\perp\text{-quasi-periodic over } \partial\Omega \end{array}\right\}, \tag{28}$$

$$\mathcal{W} = \left\{\begin{array}{l} \boldsymbol{F}_\perp \in (L^2(\Omega))^2 \mid \nabla_\perp \times \boldsymbol{F}_\perp \in L^2(\Omega); \\ \boldsymbol{F}_\perp \cdot \vec{\tau} \text{ is } \boldsymbol{k}_\perp\text{-quasi-periodic over } \partial\Omega \end{array}\right\}. \tag{29}$$

Then if we multiply the first and second equations in Eq. (26) respectively by the complex conjugate of the test functions $\boldsymbol{F}_\perp \in \mathcal{W}$ and $F_z \in \mathcal{V}$, we obtain the variational formulation of the problem after integration by parts:

Find $\zeta \in \mathbb{C}$ *and* $(\boldsymbol{E}_\perp, \hat{E}_z) \in \mathcal{W} \times \mathcal{V}$ *such that* $(\boldsymbol{E}_\perp, \hat{E}_z) \neq 0$ *and* $\forall (\boldsymbol{F}_\perp, F_z) \in \mathcal{W} \times \mathcal{V}$

$$\left\{\begin{array}{l} ((\nabla_\perp \times \boldsymbol{F}_\perp), \mu^{-1}(\nabla_\perp \times \boldsymbol{E}_\perp)) - k^2\,(\boldsymbol{F}_\perp, \varepsilon \boldsymbol{E}_\perp) \\ \qquad\qquad = \zeta^2 \left(\boldsymbol{F}_\perp, \mu^{-1}(\nabla_\perp \hat{E}_z - \boldsymbol{E}_\perp)\right), \\ (\nabla_\perp F_z, \mu^{-1}\boldsymbol{E}_\perp) - \left(\nabla_\perp F_z, \mu^{-1}\nabla_\perp \hat{E}_z\right) \\ \qquad\qquad + k^2 \left(F_z, \varepsilon \hat{E}_z\right) = 0, \end{array}\right. \tag{30}$$

where $(,)$ represents the $L^2(\Omega)$ inner product

$$(\boldsymbol{F}, \boldsymbol{E}) \;=\; \int_\Omega \overline{\boldsymbol{F}} \cdot \boldsymbol{E}\, dA\,. \tag{31}$$

2.B.3. Finite element discretization

Let $\mathcal{V}_h$ and $\mathcal{W}_h$ be two finite dimensional approximation spaces to the functional spaces $\mathcal{V}$ and $\mathcal{W}$ respectively. The discretized problem is obtained by substituting $\mathcal{W}_h \times \mathcal{V}_h$ for $\mathcal{W} \times \mathcal{V}$ in the formulation of problem (30). We introduce sets of basis functions, respectively for the spaces $\mathcal{V}_h$ and $\mathcal{W}_h$, and map these onto Eq. (30) to derive the discretized problem in matrix form [20]:

$$\left[\begin{array}{cc} \boldsymbol{K}_{tt} & \boldsymbol{0} \\ \boldsymbol{K}_{zt} & \boldsymbol{K}_{zz} \end{array}\right] \left[\begin{array}{c} \boldsymbol{E}_{\perp,n} \\ \hat{\boldsymbol{E}}_{z,n} \end{array}\right] = \zeta_n^2 \left[\begin{array}{cc} \boldsymbol{M}_{tt} & \boldsymbol{K}_{zt}^H \\ \boldsymbol{0} & \boldsymbol{0} \end{array}\right] \left[\begin{array}{c} \boldsymbol{E}_{\perp,n} \\ \hat{\boldsymbol{E}}_{z,n} \end{array}\right], \tag{32}$$

where the superscript H denotes the Hermitian transpose (or conjugate transpose) operator. Let $(\boldsymbol{G}_{\perp,i})_{i\in\{1,2,\ldots,\dim(\mathcal{W}_h)\}}$ and $(\hat{G}_{z,i})_{i\in\{1,2,\ldots,\dim(\mathcal{V}_h)\}}$ be the chosen basis functions for the spaces $\mathcal{W}_h$ and $\mathcal{V}_h$ respectively. For $i, j \in \{1, 2, \ldots, \dim(\mathcal{W}_h)\}$, the elements of the matrices $\boldsymbol{K}_{tt}$ and $\boldsymbol{M}_{tt}$ are defined as

$$(\boldsymbol{K}_{tt})_{ij} \;=\; \left((\nabla_\perp \times \boldsymbol{G}_{\perp,i}), \mu^{-1}(\nabla_\perp \times \boldsymbol{G}_{\perp,j})\right) - k^2 \left(\boldsymbol{G}_{\perp,i}, \varepsilon \boldsymbol{G}_{\perp,j}\right) \tag{33}$$

$$(\boldsymbol{M}_{tt})_{ij} \;=\; -\left(\boldsymbol{G}_{\perp,i}, \mu^{-1}(\nabla_\perp \boldsymbol{G}_{\perp,j})\right), \tag{34}$$

and, for $i \in \{1, 2, \ldots, \dim(\mathcal{V}_h)\}$ and $j \in \{1, 2, \ldots, \dim(\mathcal{W}_h)\}$, the matrix $\boldsymbol{K}_{zt}$ is defined as

$$(\boldsymbol{K}_{zt})_{ij} \;=\; \left(\nabla_\perp \hat{G}_{z,i}, \mu^{-1} \boldsymbol{G}_{\perp,j}\right), \tag{35}$$

while, for $i, j \in \{1, 2, \ldots, \dim(\mathcal{V}_h)\}$, the coefficients of the matrix $\boldsymbol{K}_{zz}$ are

$$(\boldsymbol{K}_{zz})_{ij} \;=\; -\left(\nabla_\perp \hat{G}_{z,i}, \mu^{-1} \nabla_\perp \hat{G}_{z,j}\right) + k^2 \left(\hat{G}_{z,i}, \varepsilon \hat{G}_{z,j}\right). \tag{36}$$

The generalized eigenvalue problem Eq. (32) can be solved efficiently using the eigensolver for sparse matrices ARPACK [21]. Once the array modes $\boldsymbol{E}_n$ are computed, we express a field $\boldsymbol{E}$ inside the array by the modal expansion

$$\boldsymbol{E}(x, y, z) \;=\; \sum_n c_n\, \boldsymbol{E}_n(x, y)\, \exp(i\, \zeta_n\, z) \tag{37}$$

where the index n counts out all the upward and downward propagating modes.

In contrast, a formulation of Maxwell's equations which is based on (E_z, H_z) fields leads to a nonlinear eigenvalue problem [16] which becomes inefficient to solve as the number of eigenvalues to be computed increases. The ARPACK library can be used to compute a few selected eigenvalues of large sparse matrices, and a shift and invert spectral transformation can be applied so that the numerical solutions converge to eigenvalues located within a

desired region of the spectrum. Here, by considering the plane wave dispersion relation Eq. (11), the target region includes the propagation constant ζ near a reference value $\zeta_{\text{ref}} = (n_{\text{ref}}^2 k^2 - \alpha_0^2 - \beta_0^2)^{1/2}$ where the reference index $n_{\text{ref}} \in \mathbb{R}$ is selected to be slightly higher than the largest real part of the slab refractive indices.

We have chosen $\mathcal{V}_h$ as the space of two-dimensional vector fields whose components are piecewise polynomials of degree p while $\mathcal{W}_h$ consists of piecewise continuous polynomials of degree $p+1$ (in this paper $p = 2$). The vector fields of $\mathcal{V}_h$ must be tangentially continuous across the inter-element edges of the finite element triangulation while their normal component is allowed to be discontinuous (*edge element*).

We now present some general principles which have guided our choice for the spaces $\mathcal{V}_h$ and $\mathcal{W}_h$. It is known that, for a simply connected domain Ω, the gradient, curl and div operators form an *exact sequence*:

$$H(\text{Grad}, \Omega) \overset{\nabla}{\to} H(\text{Curl}, \Omega) \overset{\nabla\times}{\to} H(\text{Div}, \Omega) \overset{\nabla\cdot}{\to} L(\Omega) \tag{38}$$

i.e., the range of each operator coincides with the kernel of the following one. The derivation of this statement is based on the Poincaré lemma and for more details see Ref. [22, p. 133], for instance. For the sake of numerical stability [23], FEM approximation spaces must be chosen such that the exact sequence is reproduced at the discrete level.

In the context of waveguide mode theory, a scalar function takes the form $\left(F_z(x,y)\, e^{i\,\zeta\, z}\right)$ and its gradient is $\nabla \left(F_z(x,y)\, e^{i\,\zeta\, z}\right) = \left[\nabla_\perp F_z(x,y),\, i\,\zeta\, F_z(x,y)\right] e^{i\,\zeta\, z}$. If $F_z(x,y)$ is a piecewise continuous polynomial of degree $p+1$, i.e., $F_z(x,y) \in \mathcal{W}_h$, then the two components of $\nabla_\perp F_z(x,y)$ are piecewise polynomials of degree p, i.e., $\nabla_\perp F_z(x,y) \in \mathcal{V}_h$. We can then verify that, with our choice of $\mathcal{V}_h$ and $\mathcal{W}_h$, the first exactness relation of Eq. (38), i.e., $H(\text{Grad}, \Omega) \overset{\nabla}{\to} H(\text{Curl}, \Omega)$, is also reproduced at the discrete level. We do not discuss the second exactness relation since, here, we do not have to build an approximation space for $H(\text{Div}, \Omega)$. We recall that in this paper we set $p = 2$, and approximate the transverse and longitudinal components using polynomials of degrees 2 and 3 respectively; the construction of the basis functions for the FEM spaces is described in Ref. [20].

2.B.4. Adjoint modes and the biorthogonality property

Modal orthogonality relations, or more correctly biorthogonality relations, in the case of the problem considered here, are important in determining the field expansion coefficients c_n in Eq. (37). Although we may recast Eq. (32) in a form in which each matrix is Hermitian (for the lossless case):

$$\begin{bmatrix} \boldsymbol{K}_{tt} & \boldsymbol{0} \\ \boldsymbol{0} & \boldsymbol{0} \end{bmatrix} \begin{bmatrix} \boldsymbol{E}_{\perp,n} \\ \hat{\boldsymbol{E}}_{z,n} \end{bmatrix} = \zeta_n^2 \begin{bmatrix} \boldsymbol{M}_{tt} & \boldsymbol{K}_{zt}^H \\ \boldsymbol{K}_{zt} & \boldsymbol{K}_{zz} \end{bmatrix} \begin{bmatrix} \boldsymbol{E}_{\perp,n} \\ \hat{\boldsymbol{E}}_{z,n} \end{bmatrix}, \tag{39}$$

this generalized eigenvalue problem $\boldsymbol{A}\,\boldsymbol{v} = \zeta^2\,\boldsymbol{B}\,\boldsymbol{v}$ is not Hermitian in general, since for two Hermitian matrices, $\boldsymbol{A}$ and $\boldsymbol{B}$, the corresponding eigenproblem, $\boldsymbol{B}^{-1}\,\boldsymbol{A}\,\boldsymbol{v} = \zeta^2\,\boldsymbol{v}$ is not necessarily Hermitian since the product of two Hermitian matrices is not, in general, Hermitian. Accordingly, the eigenmodes $\boldsymbol{E}_n$ do not necessarily form an orthogonal set. It is also clear that the eigenproblem is not Hermitian in the presence of loss.

Therefore we introduce the adjoint problem that we solve to obtain a set of adjoint modes which have a biorthogonality property [18] with respect to the eigenmodes $\boldsymbol{E}_n$. In order to define the adjoint operators, we first write Eq. (27), the alternate form of Eq. (26), as

$$\mathcal{L}\,\boldsymbol{E}_n \;=\; \zeta_n^2 \mathcal{M}\,\boldsymbol{E}_n, \tag{40}$$

where $\mathcal{L}$ and $\mathcal{M}$ are the differential operators defined by

$$\mathcal{L}\,\boldsymbol{E} = \begin{bmatrix} \vec{\nabla}_\perp \times (\mu^{-1}(\nabla_\perp \times \boldsymbol{E}_\perp)) - k^2\varepsilon \boldsymbol{E}_\perp & 0 \\ 0 & 0 \end{bmatrix}, \tag{41}$$

$$\mathcal{M}\,\boldsymbol{E} = \begin{bmatrix} -\mu^{-1}\boldsymbol{E}_\perp & \mu^{-1}\nabla_\perp \hat{E}_z \\ -\nabla_\perp\cdot(\mu^{-1}\boldsymbol{E}_\perp) & \nabla_\perp\cdot(\mu^{-1}\nabla_\perp \hat{E}_z) + k^2\varepsilon \hat{E}_z \end{bmatrix}. \tag{42}$$

The adjoint operators $\mathcal{L}^\dagger$ and $\mathcal{M}^\dagger$, with respect to the inner product Eq. (31) are

$$\mathcal{L}^\dagger \boldsymbol{F} = \begin{bmatrix} \vec{\nabla}_\perp \times (\overline{\mu}^{-1}(\nabla_\perp \times \boldsymbol{F}_\perp)) - k^2\overline{\varepsilon} \boldsymbol{F}_\perp & 0 \\ 0 & 0 \end{bmatrix}, \tag{43}$$

$$\mathcal{M}^\dagger \boldsymbol{F} = \begin{bmatrix} -\overline{\mu}^{-1}\boldsymbol{F}_\perp & \overline{\mu}^{-1}\nabla_\perp \hat{F}_z \\ -\nabla_\perp\cdot(\overline{\mu}^{-1}\boldsymbol{F}_\perp) & \nabla_\perp\cdot(\overline{\mu}^{-1}\nabla_\perp \hat{F}_z) + k^2\overline{\varepsilon} \hat{F}_z \end{bmatrix}, \tag{44}$$

and follow from the definitions

$$\left(\mathcal{L}^\dagger \boldsymbol{F}, \boldsymbol{E}\right) \;=\; \left(\boldsymbol{F}, \mathcal{L}\,\boldsymbol{E}\right), \quad \forall \boldsymbol{E}, \boldsymbol{F}, \tag{45}$$

$$\left(\mathcal{M}^\dagger \boldsymbol{F}, \boldsymbol{E}\right) \;=\; \left(\boldsymbol{F}, \mathcal{M}\,\boldsymbol{E}\right), \quad \forall \boldsymbol{E}, \boldsymbol{F}. \tag{46}$$

Although for lossless media, we then have $\mathcal{L}^\dagger = \mathcal{L}$ and $\mathcal{M}^\dagger = \mathcal{M}$, as in Eq. (39), eigenproblem Eq. (40) is not Hermitian and, as we see in Section 3, complex values of ζ_n^2 can occur even for a lossless photonic crystal.

The modes $\boldsymbol{E}_n^c$ are the eigenmodes of the problem

$$\mathcal{L}^\dagger \boldsymbol{E}_m^c \;=\; \zeta_m^{c\,2} \mathcal{M}^\dagger \boldsymbol{E}_m^c \tag{47}$$

which satisfy the same quasi-periodic boundary conditions as $\boldsymbol{E}_n$.

We now conjugate the boundary value problem Eq. (47) and take into account the fact that $\mathcal{L}^\dagger = \overline{\mathcal{L}}$ and $\mathcal{M}^\dagger = \overline{\mathcal{M}}$. Consistent with Eqs (17) and (18) we redefine the adjoint mode as the eigenmode $\boldsymbol{E}_m^\dagger$ which satisfies the same partial differential equation as $\boldsymbol{E}_n$, i.e.,

$$\mathcal{L}\,\boldsymbol{E}_m^\dagger \;=\; \zeta^{\dagger\,2}_m \mathcal{M}\,\boldsymbol{E}_m^\dagger, \tag{48}$$

but with the quasi-periodic boundary conditions associated with the adjoint wavevector $\boldsymbol{k}_\perp^\dagger = -\boldsymbol{k}_\perp$. This is convenient for the FEM programming since the same subprograms can be used to handle the partial differential equations (40) and (48) while only a few lines of code are needed to manage the sign change for $\boldsymbol{k}_\perp$.

The spectral theory for non-self-adjoint operators is difficult and in general less developed. In this paper we assume that the modes $\boldsymbol{E}_n$ form a complete set and that the adjoint modes $\boldsymbol{E}_n^\dagger$ can be numbered such that $\zeta_n^{\dagger 2} = \zeta_n^2$, and the following biorthogonality relationship is satisfied

$$\int_\Omega \boldsymbol{e}_z \cdot (\boldsymbol{E}_m^\dagger \times \boldsymbol{H}_n) dA \;\; = \;\; \delta_{mn}, \tag{49}$$

in which $\boldsymbol{H} = [\boldsymbol{H}_\perp, H_z]$ can be obtained from the electric field $\boldsymbol{E} = [\boldsymbol{E}_\perp, E_z]$ using the relation

$$\boldsymbol{H} \;\; = \;\; \frac{\nabla \times \boldsymbol{E}}{i\, k\, \mu} \tag{50}$$

which is derived directly from Maxwell's equations (14).

A similar spectral property has been proven for a class of non-self-adjoint Sturm-Liouville problems (see for instance, Theorem 5.3 of Ref. [24]). It is not clear if such a theorem can be extended to the vectorial waveguide mode problem, although it has been shown that the spectral theory of compact operators can be applied to a waveguide problem [19]. However, our numerical calculations have generated modes which satisfy the biorthogonality relation and verify the completeness relations Eqs (107) and (111), in Appendix B, to generally within 10^{-4}, and with even a better convergence when the number of plane wave orders and array modes, used in the truncated expansion, increase.

We now establish the biorthogonality relation Eq. (49) using the operator definitions Eqs. (45) and (46) of the adjoint, and Eqs (40) and (48). This relation may also be established directly from Maxwell's equations, as is shown in Appendix A.

We begin with

$$\left(\mathcal{L}^\dagger \overline{\boldsymbol{E}_m^\dagger}, \boldsymbol{E}_n\right) \;\; = \;\; \left(\overline{\boldsymbol{E}_m^\dagger}, \mathcal{L}\, \boldsymbol{E}_n\right), \tag{51}$$

and, since $\boldsymbol{E}_n$ and $\boldsymbol{E}_m^\dagger$ are eigenfunctions, we obtain

$$\left(\overline{\zeta_m^\dagger}^2 \mathcal{M}^\dagger \overline{\boldsymbol{E}_m^\dagger}, \boldsymbol{E}_n\right) \;\; = \;\; \left(\overline{\boldsymbol{E}_m^\dagger}, \zeta_n^2 \mathcal{M}\, \boldsymbol{E}_n\right). \tag{52}$$

Now, by taking into account Eq. (46), we can derive the following biorthogonality property:

$$\left(\zeta_n^2 - \zeta_m^{\dagger\, 2}\right) \left(\overline{\boldsymbol{E}_m^\dagger}, \mathcal{M}\, \boldsymbol{E}_n\right) \;\; = \;\; 0\,, \tag{53}$$

i.e.,

$$\left(\overline{\boldsymbol{E}_m^\dagger}, \mathcal{M}\,\boldsymbol{E}_n\right) \;=\; 0, \quad \text{if } \zeta_n^2 \neq {\zeta_m^\dagger}^2 . \tag{54}$$

The integrand of the field product in Eq. (54) can be expressed in term of the fields $\boldsymbol{H}_m$ and $\boldsymbol{E}_n^\dagger$ as in Eq. (49) by noting

$$\begin{aligned} \boldsymbol{e}_z \cdot (\boldsymbol{E}_m^\dagger \times \boldsymbol{H}_n) &= \frac{\boldsymbol{E}_{m,\perp}^\dagger \cdot (i\,\zeta_n\,\boldsymbol{E}_{n,\perp} - \nabla_\perp E_{n,z})}{i\,k\,\mu} && (55)\\ &= -\frac{\zeta\,\boldsymbol{E}_{m,\perp}^\dagger \cdot (\mathcal{M}\,\boldsymbol{E}_n)_\perp}{k}, && (56)\\ &= -\frac{\zeta\,\boldsymbol{E}_m^\dagger \cdot (\mathcal{M}\,\boldsymbol{E}_n)}{k}, && (57) \end{aligned}$$

since $(\mathcal{M}\,\boldsymbol{E}_n)_z = 0$, (40) and (41).

The biorthogonality relation Eq. (54) is useful for the FEM implementation of the field product since the product of two vectors $\boldsymbol{v}$ and $\boldsymbol{v}^\dagger$ takes the form $-\zeta\,(\boldsymbol{v}^\dagger \cdot (\boldsymbol{M}\,\boldsymbol{v}))/k$ where $\boldsymbol{M}$ is the discrete version of the operator $\mathcal{M}$ and is the matrix on the right hand side of Eq. (39).

The calculation of the modes $\boldsymbol{E}_n$ and the adjoint modes $\boldsymbol{E}_n^\dagger$ using this FEM approach is highly efficient and numerically stable.

In the following section we use modes of the structure for the field expansion inside the photonic crystal slab, and exploit the adjoint modes, which are biorthogonal to the primal modes, in the solution of the field matching problem in a least square sense.

2.C. Fresnel interface reflection and transmission matrices

In this section we introduce the Fresnel reflection and transmission matrices for photonic crystal-air interfaces and calculate the total transmission, reflection and absorption of a photonic crystal slab. First we introduce the Fresnel reflection $\boldsymbol{R}_{12}$ and transmission $\boldsymbol{T}_{12}$ matrices for an interface between free space and the semi-infinite array of cylinders. We specify an incident plane wave field $\boldsymbol{f}^{E/M-}$ (see Eqs(9)–(10)) propagating from above onto a semi-infinite slab, giving rise to an upward reflected plane wave field $\boldsymbol{f}^{E/M+}$ and a downward propagating field of modes $\boldsymbol{c}^-$ in the slab.

The field matching equations between the plane wave expansions Eqs (9) and (10) and the array mode expansion Eq. (37) are obtained by enforcing the continuity of the tangential

components of transverse fields on either side of the interface:

$$\sum_s \chi_s^{-1/2} \left(f_s^{E-} + f_s^{E+}\right) \boldsymbol{R}_s^E + \chi_s^{1/2} \left(f_s^{M-} + f_s^{M+}\right) \boldsymbol{R}_s^M = \sum_n c_n^- \boldsymbol{E}_{n\perp}, \tag{58}$$

$$\sum_s \chi_s^{1/2} \left(f_s^{E-} - f_s^{E+}\right) \boldsymbol{R}_s^E + \chi_s^{-1/2} \left(f_s^{M-} - f_s^{M+}\right) \boldsymbol{R}_s^M = \sum_n c_n^- \left(\boldsymbol{e}_z \times \boldsymbol{H}_{n\perp}\right). \tag{59}$$

Equations (58) and (59) correspond to the continuity condition of the tangential electric field and magnetic field respectively. Here $\boldsymbol{E}_{n\perp}$ denotes the downward tangential electric field component of mode n while $\boldsymbol{H}_{n\perp}$ denotes the downward tangential magnetic field of mode n, which satisfy the orthonormality relation

$$\int_\Omega \boldsymbol{e}_z \cdot (\boldsymbol{E}_m^\dagger \times \boldsymbol{H}_n) dA = -\delta_{mn}. \tag{60}$$

In Appendix B we derive completeness relations for both the Bloch modes basis and the plane wave basis.

We now proceed to solve these equations in a least squares sense, using the Galerkin-Rayleigh-Ritz method in which the two sets of equations are respectively projected on the two sets of basis functions. In this treatment, we project the electric field equation onto the plane wave basis and the magnetic field equation onto the slab mode basis to derive, in matrix form,

$$\boldsymbol{X}^{-1/2} \left(\boldsymbol{f}^- + \boldsymbol{f}^+\right) = \boldsymbol{J}\boldsymbol{c}^-, \tag{61}$$

$$\boldsymbol{J}^\dagger \boldsymbol{X}^{1/2} \left(\boldsymbol{f}^- - \boldsymbol{f}^+\right) = \boldsymbol{c}^-, \tag{62}$$

where

$$\boldsymbol{f}^\pm = \begin{pmatrix} \boldsymbol{f}^{E\pm} \\ \boldsymbol{f}^{M\pm} \end{pmatrix}, \quad \boldsymbol{X} = \begin{pmatrix} \boldsymbol{\chi} & \boldsymbol{0} \\ \boldsymbol{0} & \boldsymbol{\chi}^{-1} \end{pmatrix}, \tag{63}$$

$$\boldsymbol{J} = \begin{pmatrix} \boldsymbol{J}^E \\ \boldsymbol{J}^M \end{pmatrix}, \qquad \boldsymbol{J}^{E/M} = \left[J_{sm}^{E/M}\right],$$

$$J_{sm}^{E/M} = \iint \overline{\boldsymbol{R}}_s^{E/M} \cdot \boldsymbol{E}_{m\perp}\, dS, \tag{64}$$

$$\boldsymbol{J}^\dagger = \begin{pmatrix} \boldsymbol{J}^{\dagger E} & \boldsymbol{J}^{\dagger M} \end{pmatrix}, \qquad \boldsymbol{J}^{\dagger E/M} = \left[J_{ms}^{\dagger E/M}\right],$$

$$J_{ms}^{\dagger E/M} = \iint \boldsymbol{R}_s^{E/M} \cdot \boldsymbol{E}_{m\perp}^\dagger\, dS, \tag{65}$$

$$\boldsymbol{\chi} = \text{diag}\,\{\chi_s\}. \tag{66}$$

Then, defining the scattering matrices $\boldsymbol{R}_{12}$ and $\boldsymbol{T}_{12}$ according to the definitions

$$\boldsymbol{f}^+ = \boldsymbol{R}_{12}\boldsymbol{f}^-, \qquad \boldsymbol{c}^- = \boldsymbol{T}_{12}\boldsymbol{f}^-, \tag{67}$$

we may solve Eqs (61) and (62) to derive

$$\boldsymbol{R}_{12} = -\boldsymbol{I} + 2\boldsymbol{A}\left(\boldsymbol{I} + \boldsymbol{B}\boldsymbol{A}\right)^{-1}\boldsymbol{B} = (\boldsymbol{A}\boldsymbol{B} + \boldsymbol{I})^{-1}(\boldsymbol{A}\boldsymbol{B} - \boldsymbol{I}), \tag{68}$$

$$\begin{aligned} \boldsymbol{T}_{12} &= 2\left(\boldsymbol{I} + \boldsymbol{B}\boldsymbol{A}\right)^{-1}\boldsymbol{B}, & (69)\\ \text{where } \boldsymbol{A} &= \boldsymbol{X}^{1/2}\boldsymbol{J},\ \boldsymbol{B} = \boldsymbol{J}^\dagger\boldsymbol{X}^{1/2}. & (70) \end{aligned}$$

For a structure with inversion symmetric inclusions the following useful relations hold: $\boldsymbol{E}_n^\dagger(\boldsymbol{r}) = \boldsymbol{E}_n(-\boldsymbol{r})$, $\boldsymbol{J}^\dagger = \boldsymbol{J}^T$ and $\boldsymbol{B} = \boldsymbol{A}^T$. While the Fresnel matrices $\boldsymbol{R}_{12}$ and $\boldsymbol{T}_{12}$ given in Eqs (68) and (69) have been derived by presuming a plane wave field incident from above, identical forms are derived if we presume incidence from below, a consequence of the given symmetries of the modes.

We now derive the slab-free space Fresnel coefficients, assuming that we have a modal field $\boldsymbol{c}^-$ incident from above and giving rise to a reflected modal field $\boldsymbol{c}^+$ and a transmitted plane wave field $\boldsymbol{f}^-$ below. This time, the field matching equations are

$$\begin{aligned} \sum_s \chi_s^{-1/2} f_s^{E-}\boldsymbol{R}_s^E + \chi_s^{1/2} f_s^{M-}\boldsymbol{R}_s^M &= \\ \sum_n \left(c_n^- + c_n^+\right)\boldsymbol{E}_{n\perp}, & (71)\\ \sum_s \chi_s^{1/2} f_s^{E-}\boldsymbol{R}_s^E + \chi_s^{-1/2} f_s^{M-}\boldsymbol{R}_s^M &= \\ \sum_n \left(c_n^- - c_n^+\right)\left(\boldsymbol{e}_z \times \boldsymbol{H}_{n\perp}\right), & (72) \end{aligned}$$

and we again project the electric field equation onto the plane wave basis and the magnetic field equation on to the modal basis for the slab. Accordingly, we derive

$$\begin{aligned} \boldsymbol{X}^{-1/2}\boldsymbol{f}^- &= \boldsymbol{J}\left(\boldsymbol{c}^- + \boldsymbol{c}^+\right), & (73)\\ \boldsymbol{J}^\dagger\boldsymbol{X}^{1/2}\boldsymbol{f}^- &= \boldsymbol{c}^- - \boldsymbol{c}^+. & (74) \end{aligned}$$

Then, defining the scattering matrices $\boldsymbol{R}_{21}$ and $\boldsymbol{T}_{21}$ according to $\boldsymbol{c}^+ = \boldsymbol{R}_{21}\boldsymbol{c}^-$ and $\boldsymbol{f}^+ = \boldsymbol{T}_{21}\boldsymbol{c}^-$, we form

$$\begin{aligned} \boldsymbol{R}_{21} &= \left(\boldsymbol{I} - \boldsymbol{B}\boldsymbol{A}\right)\left(\boldsymbol{I} + \boldsymbol{B}\boldsymbol{A}\right)^{-1}, & (75)\\ \boldsymbol{T}_{21} &= 2\boldsymbol{A}\left(\boldsymbol{I} + \boldsymbol{B}\boldsymbol{A}\right)^{-1}. & (76) \end{aligned}$$

These Fresnel scattering matrices $\boldsymbol{R}_{12}$, $\boldsymbol{T}_{12}$, $\boldsymbol{R}_{21}$, $\boldsymbol{T}_{21}$ can now be readily utilized to calculate the total transmission, reflection and the absorption of the slab. Note that for inversion

symmetric inclusions the following reciprocity relations hold: $\boldsymbol{T}_{12}^T = \boldsymbol{T}_{21}$ and $\boldsymbol{R}_{12}^T = \boldsymbol{R}_{21}$. These relations hold independently of the truncation of the field expansions. In addition, in general, the following relations are also true: $\boldsymbol{T}_{12}\boldsymbol{T}_{21} = \boldsymbol{I} - \boldsymbol{R}_{21}^2$ and $\boldsymbol{T}_{21}\boldsymbol{T}_{12} = \boldsymbol{I} - \boldsymbol{R}_{12}^2$.

2.D. Transmission, reflection of the slab

Following the diagram in Fig. 2, we may use the Fresnel interface matrices to calculate the transmission and the reflection matrices for the entire structure from the following equations:

$$\boldsymbol{f}_1^+ = \boldsymbol{R}_{12}\boldsymbol{f}_1^- + \boldsymbol{T}_{21}\boldsymbol{P}\boldsymbol{c}^+, \tag{77}$$

$$\boldsymbol{c}^- = \boldsymbol{T}_{12}\boldsymbol{f}_1^- + \boldsymbol{R}_{21}\boldsymbol{P}\boldsymbol{c}^+, \tag{78}$$

$$\boldsymbol{c}^+ = \boldsymbol{R}_{21}\boldsymbol{P}\boldsymbol{c}^-, \tag{79}$$

$$\boldsymbol{f}_2^- = \boldsymbol{T}_{21}\boldsymbol{P}\boldsymbol{c}^-, \tag{80}$$

where $\boldsymbol{P} = \mathrm{diag}\,[\exp(i\,\zeta_n\,h)]$ is the diagonal matrix which describes the propagation of the n^{th} Bloch mode inside the slab with a thickness h. The transmission and reflection matrices defined as $\boldsymbol{f}_2^- = \boldsymbol{T}\boldsymbol{f}_1^-$, $\boldsymbol{f}_1^+ = \boldsymbol{R}\boldsymbol{f}_1^-$ can be deduced from the system Eqs. (77)–(80) as

$$\boldsymbol{T} = \boldsymbol{T}_{21}\boldsymbol{P}(\boldsymbol{I} - \boldsymbol{R}_{21}\boldsymbol{P}\boldsymbol{R}_{21}\boldsymbol{P})^{-1}\boldsymbol{T}_{12}, \tag{81}$$

$$\boldsymbol{R} = \boldsymbol{R}_{12} + \boldsymbol{T}_{21}\boldsymbol{P}(\boldsymbol{I} - \boldsymbol{R}_{21}\boldsymbol{P}\boldsymbol{R}_{21}\boldsymbol{P})^{-1}\boldsymbol{R}_{21}\boldsymbol{P}\boldsymbol{T}_{12}. \tag{82}$$

The amplitudes of the transmitted and reflected fields are then given by, $\boldsymbol{t} = \boldsymbol{T}\boldsymbol{\delta}$, $\boldsymbol{r} = \boldsymbol{R}\boldsymbol{\delta}$, where $\boldsymbol{\delta} = [0, \ldots, 0, \cos\delta, 0, \ldots, 0, \sin\delta, 0, \ldots, 0]^T$ is the vector containing the magnitudes of components of the incident plane wave in the specular diffraction order, and δ is the angle between the electric vector and the plane of incidence. The absorptance, A, is calculated by energy conservation as

$$A = 1 - \sum_{s\in\mathcal{P}}[|r_s|^2 + |t_s|^2], \tag{83}$$

where r_s, t_s are the diffraction order components of $\boldsymbol{r}$, $\boldsymbol{t}$ and $\mathcal{P}$ is the set of all propagating orders in free space.

In the absence of absorption the following relations for the slab reflection $\boldsymbol{R}$ and transmission $\boldsymbol{T}$ matrices can be deduced (for details see Appendix C). Given that the photonic crystal slab is up/down symmetric, the slab transmission $\boldsymbol{T}'$ and the reflection $\boldsymbol{R}'$ matrices for plane wave incidence from below are the same as for incidence from above: $\boldsymbol{T}' = \boldsymbol{T}$ and $\boldsymbol{R}' = \boldsymbol{R}$. Therefore the energy conservation relations take the form

$$\boldsymbol{R}^{\mathrm{H}}\boldsymbol{I}_1\boldsymbol{R} + \boldsymbol{T}^{\mathrm{H}}\boldsymbol{I}_1\boldsymbol{T} = \boldsymbol{I}_1 + i\boldsymbol{R}^{\mathrm{H}}\boldsymbol{I}_{\overline{1}} - i\boldsymbol{I}_{\overline{1}}\boldsymbol{R}, \tag{84}$$

$$\boldsymbol{R}^{\mathrm{H}}\boldsymbol{I}_1\boldsymbol{T} + \boldsymbol{T}^{\mathrm{H}}\boldsymbol{I}_1\boldsymbol{R} = i\boldsymbol{T}^{\mathrm{H}}\boldsymbol{I}_{\overline{1}} - i\boldsymbol{I}_{\overline{1}}\boldsymbol{T}, \tag{85}$$

with $\boldsymbol{I}_1$ denoting a diagonal matrix with the entries 1 for the propagating plane wave channels and zeros for the evanescent plane wave channels, and $\boldsymbol{I}_{\overline{1}}$ being a diagonal matrix which has entries $+1$ in the evanescent TE channels and -1 in the evanescent TM channels, and zeros for the propagating channels.

The semi-analytic expressions for the transmission Eq. (81) and the reflection Eq. (82) matrices for the slab can give important insight to improve the overall absorption efficiency. For instance, in Eq. (81) the matrices $\boldsymbol{T}_{12}$ and $\boldsymbol{T}_{21}$ represent the coupling matrices for a plane wave into and out of the slab, while the scattering matrix

$$(\boldsymbol{I} - \boldsymbol{R}_{21}\boldsymbol{P}\boldsymbol{R}_{21}\boldsymbol{P})^{-1} \tag{86}$$

describes Fabry-Perot-like multiple scattering. As demonstrated in Ref. [25], absorption is enhanced if first, there is a strong coupling ($\boldsymbol{T}_{12}$), strong scattering amplitudes Eq. (86) that increase the effective path in the slab multiple times, and the field strength is concentrated in the region of high absorption.

3. Numerical simulations and verifications

In this section, we first use our mode solver to compute the dispersion curves of an array of lossless cylinders. Then we apply our modal approach to analyze the absorption spectrum of an array of lossy cylinders (silicon) and we also examine the convergence of the method with respect to the truncation parameters. Finally, we consider the example of a photonic crystal slab which exhibits Fano resonances.

3.A. Dispersion curves of an array of cylinders

Though our method can be applied to inclusions of any cross section, we first consider an array of lossless circular cylinders, with dielectric constant $n_c^2 = 8.9$ (alumina), and normalized radius $a/d = 0.2$, in an air background (refractive index $n_b = 1$). We compute the propagation constant ζ of the Bloch modes defined in Eq. (20) using the vectorial FEM.

Figure 3 shows the dispersion curves corresponding to a periodic boundary condition in the transverse plane, i.e., $\boldsymbol{k}_\perp = (\alpha_0, \beta_0) = (0, 0)$. The solid red curves indicate values of the propagation constant ζ such that ζ^2 is real—with positive values of ζ^2 corresponding to propagating modes, while negative values indicate evanescent modes.

The dispersion curve for the fundamental propagating mode is at the lower right corner and starts at the coordinate origin. Complex values of ζ^2 can also occur, even for a lossless system, and even with $\operatorname{Re}\zeta^2 > 0$; these modes, which occur in conjugate pairs, are shown by the dashed blue curves and are distinguished by a horizontal axis which is labeled $\operatorname{Re}\zeta^2 + \operatorname{Im}\zeta^2$. We can observe that the dashed blue curves connect a maximum point of a solid red curve to a minimum point of another solid red curve. This property of the dispersion of cylinders arrays was observed by Blad and Sudbø [16].

The dispersion curves in Fig. 3 are plotted using the same parameters as in Fig. 4 of Ref. [16]. All curves shown in Fig. 4 of [16] also appear in Fig. 3 of the present paper although our figure reveals many additional curves, for instance, near $((\mathrm{Re}\,\zeta^2 + \mathrm{Im}\,\zeta^2)/(2\,\pi/d)^2, d^2/\lambda^2) = (-2., 0.1)$. In [16], the dispersion curves were plotted using a continuation method whose starting points are on the axis $\zeta = 0$; most of the curves which do not intersect this axis are missing in Fig. 4 of [16] but their solutions are required for the completeness of the modal expansion Eqs (58) and (59). For instance, if the eigenvalues ζ_n are numbered in decreasing order of $\mathrm{Re}\,\zeta_n^2$, then the index number of the eigenvalues, which appear near $((\mathrm{Re}\,\zeta^2 + \mathrm{Im}\,\zeta^2)/(2\,\pi/d)^2, d^2/\lambda^2) = (-2.0, 0.1)$ in Fig. 3, are between 10 and 20 and, as explained in the convergence study of the next section, we typically need well over 20 modes to obtain good convergence.

3.B. Absorptance of a dilute silicon nanowire array

We now consider a silicon nanowire (SiNW) array consisting of absorptive nanowires of radius $a = 60\,\mathrm{nm}$, arranged in square lattice of lattice constant $d = 600\,\mathrm{nm}$. This constitutes a dilute SiNW array since the silicon fill fraction is approximately 3.1%. The dilute nature of the array can facilitate the identification of the modes which play a key role in the absorption mechanism [25]. The height of the nanowires is $h = 2.33\,\mu\mathrm{m}$. For silicon we use the complex refractive index of Green and Keevers [26]. Figure 4 shows the absorptance spectrum of the dilute SiNW array, together with the absorptance of a homogeneous slab of equivalent thickness and of a homogeneous slab of equivalent volume of silicon. The absorption feature between 600 and 700 nm is absent in bulk silicon and is entirely due to the nanowire geometry. Using our method we have identified some specific Bloch modes which play a key role in this absorption behavior [25]. At shorter wavelengths the absorption of the silicon is high and therefore the absorption of the slab does not depend on the slab thickness (see Fig.4 thin blue curve and thick red curve).

Note that that the geometry of the inclusion does not need to be circular since our FEM based method can handle arbitrary inclusion shapes. Indeed, in Fig. 5 the absorptance spectrum of a SiNW array consisting of square cylinders is analyzed and compared to the absorptance for circular cylinders of same period and cross sectional area. At long wavelengths, the absorption for the two geometries is the same, while at shorter wavelengths the absorption is slightly higher for the square cylinders. This can be explained by the field concentration at the corners of the square cylinders [27].

The contour plot in Fig. 6 shows the absorptance versus wavelength and the cylinder height h for the circular SiNW array. Note that the nanowire height of $h = 2.33\,\mu\mathrm{m}$ used in Fig. 4 is, indeed, in a region of high absorptance for the wavelength band $[600\,\mathrm{nm}, 700\,\mathrm{nm}]$. Note that the propagation matrix $\boldsymbol{P}$ is the only matrix in the expressions (81) and (82) for

the reflection and transmission matrices which depends on the thickness h and it can be easily updated when h is varied for a fixed value of the wavelength. Thus, the modal method is a very fast technique in exploring the dependence of the absorptance with respect to the thickness. Indeed, the contour plot is obtained by computing the absorptance for 6001 height values uniformly spaced over the interval $[0\,\mu\text{m}, 3\,\mu\text{m}]$, for 409 wavelength values uniformly distributed over the interval $[310\,\text{nm}, 1126\,\text{nm}]$; a high sampling resolution is required in order to capture the oscillatory features which occur in the region $\lambda \in [400\,\text{nm}, 700\,\text{nm}]$. It took about 44 hours to generate the full results using 16 cores of a high performance parallel computer with 256 cores (it is a shared memory system consisting of 128 processors Intel Itanium 2 1.6GHz (Dual Core)). If the absorptance had to be computed independently for the 6001×409 data points, this would have required many months of computer time.

We have studied the convergence with respect to the truncation parameters of the plane wave expansions and array mode expansions in Eqs (58) and (59). The array modes are ordered in decreasing order with respect to $\text{Re}\,\zeta_n^2$. We have used a *circular truncation* for the plane wave truncation number N_{PM}, i.e., for a given value of N_{PM}, only the plane wave orders (p, q) such that $p^2 + q^2 \leq N_{\text{PM}}^2$ are used in the truncated expansions; this choice is motivated by the fact that, for normal incidence, it is consistent with the ordering of the array modes since the plane wave propagation constants are given by the dispersion relation $\gamma_s^2 = k^2 - (p^2 + q^2)\,(2\pi/d)^2$ (see Eq. (11)); the propagation constants γ_s are also numbered in decreasing value of $-(p^2 + q^2)$.

Figures 7 and 8 illustrate the convergence when the number of plane wave orders and the number of array modes used in modal expansions are increased. The wavelength is set to $\lambda = 700\,\text{nm}$ and the corresponding silicon refractive index is $n = 3.774 + 0.011\,i$, which is taken from Ref. [26]. The error is estimated by assuming that the result obtained with the highest discretization is "exact" ($A = 0.13940$ for $N_{\text{PM}} = 10$ and $N_{\text{array}} = 160$). The calculations are based on a highly refined FEM mesh consisting of 8088 triangles and 16361 nodes. In Fig. 8, there is a sudden jump in error when $N_{\text{array}} = 120$ (isolated blue dot); this is due to the chosen truncation cutting through a pair of degenerate eigenvalue $\zeta_{120} = \zeta_{121}$ i.e., including one member of the pair but excluding the other). Indeed the solution is well-behaved when $N_{\text{array}} = 121$. Similar behavior has been observed when a pair of conjugate eigenvalues is cut. Thus all members of a family of eigenvalues must be included together in the modal expansion, otherwise there is degradation of the convergence, which is particularly strong when it occurs for a low-order eigenvalue which makes a significant contribution to the modal expansions. In practice we expect the computed absorptance to have about three digits of accuracy when the truncation parameters of the plane wave expansions and array mode expansions are set respectively to $N_{\text{PM}} = 3$ (giving 29 plane wave orders and 2×29 basis functions for TE and TM polarizations) and $N_{\text{array}} = 50$, assuming adequate resolution

of the FEM mesh. The absorptance curve for the dilute SiNW array in Fig. 4 is obtained using these truncation parameters and an FEM mesh which has 1982 triangles and 4061 nodes.

Figure 9 presents the absorptance spectrum for off-normal incidence (45°). The absorptance is sensitive to the angle of incidence and the light polarization. Compared with normal incidence, the absorptance peak in the wavelength band [600 nm, 700 nm] (low silicon absorption) has shifted to shorter wavelengths while the peak near 400 nm (high silicon absorption) has shifted to longer wavelengths.

3.C. Fano resonances in a photonic crystal slab

Fano resonances are well known from the field of particle physics [28], and they are observable also in photonic crystals [29]. They are notable for their sharp spectral features and so serve as a good benchmark for the accuracy of new numerical methods. We have carried out a calculation of Fano resonances using our modal formulation. We present here an example that was first studied by Fan and Joannopoulos [29]. The photonic crystal slab consists of a square array of air holes in a background material of relative permittivity $\epsilon = 12$. Figure 10 shows the transmittance of a photonic crystal slab as a function of the normalized frequency d/λ for a plane wave at normal incidence. The parameters of the slab considered in Fig. 10 are identical to those in Fig. 12(a) of Ref. [29], and the curves from the two figures are the same to visual accuracy. This is an additional validation of the approach presented here. The transmittance curve reveals a strong transmission resonance which is typical of asymmetric Fano resonances. These resonances are very sharp and can be used for switching purposes [30].

4. Conclusion

We have developed a rigorous modal formulation for the diffraction of plane waves by absorbing photonic crystal slabs. This approach combines the strongest aspects of two methods: the computation of Bloch modes is handled numerically, using finite elements in a two-dimensional context where this method excels, while the reflection and transmission of the fields through the slab interfaces are handled semi-analytically, using a generalization of the theory of thin films. This approach can lead to results achieved using a fraction of the computational resources of conventional algorithms: an example of this is given in Fig. 6, in which a large number of different computations for different slab thicknesses were able to be computed in a very short time. Although the speed-testing of this method against conventional methods (FDTD and 3D Finite Element packages such as COMSOL) is a subject for future work, we have demonstrated here the method's accuracy and its rapidity of convergence. The method also satisfies all internal checks related to reciprocity and conservation of energy, as

well as reproducing known results from the literature in challenging situations, such as the simulation of Fano resonances (Fig. 10).

The method is very general with respect to the geometry of the structure. We have demonstrated this by modeling both square and circular shaped inclusions. In addition, because the method is at a fixed frequency, it can handle both dissipative and dispersive structures in a straightforward manner, using tabulated values of the real and imaginary parts of the refractive index. This is in contrast to time-domain methods such as FDTD, or to some formulations of the finite element approach. Though we have used a single array type here (the square array), other types of structure (such as hexagonal arrays) can be dealt with by appropriately adjusting the unit cell Ω, together with the allowed range of Bloch modes.

It is also easy to see how this method could be extended to multiple slabs containing different geometries, as well as taking into account the effect of one or more substrates; this extension would involve the inclusion of field expansions for each layer, together with appropriate Fresnel matrices, in the equation system (77)-(80). In principle this approach could then be used to study rods (or holes) whose radius or refractive index changed continuously with depth, provided the spacing between the array cells remained constant.

Our method has an important advantage over purely numerical algorithms in that it gives physical insight into the mechanisms of transmission and absorption in slabs of lossy periodic media. The explanation of the absorption spectrum in arrays of silicon nanorods is vital for the enhancement of efficiency of solar cells, however this spectrum is complicated, with a number of processes, including coupling of light into the structure, Fabry-Perot effects, and the overlap of the light with the absorbing material, all playing an important role. By expanding in the natural eigenmodes of each layer of the structure, it is possible to isolate these different effects and to identify criteria that the structure must satisfy in order to efficiently absorb light over a specific wavelength range. This, we have discussed in a recent related publication [25].

Acknowledgments

This research was conducted by the Australian Research Council Centre of Excellence for Ultrahigh Bandwidth Devices for Optical Systems (project number CE110001018). We gratefully acknowledge the generous allocations of computing time from the National Computational Infrastructure (NCI) and from Intersect Australia.

A. Modal biorthogonality and normalization

Here we prove the biorthogonality of the modes and adjoint modes. Let us consider set of modes $(\boldsymbol{E}_n, \boldsymbol{H}_n)$ and adjoint modes $(\boldsymbol{E}_m^\dagger, \boldsymbol{H}_m^\dagger)$ of photonic crystal. These modes satisfy

$$\nabla \times \boldsymbol{H}_n = - ik\varepsilon \boldsymbol{E}_n, \tag{87a}$$

$$\nabla \times \boldsymbol{E}_n = ik\mu \boldsymbol{H}_n \tag{87b}$$

and

$$\nabla \times \boldsymbol{H}_m^\dagger = ik\varepsilon \boldsymbol{E}_m^\dagger, \tag{88a}$$

$$\nabla \times \boldsymbol{E}_m^\dagger = - ik\mu \boldsymbol{H}_m^\dagger. \tag{88b}$$

We multiply both sides of (87a) by $\boldsymbol{E}_m^\dagger$ and (88a) by $\boldsymbol{E}_n$ and correspondingly we multiply each set of (87b) by $\boldsymbol{H}_m^\dagger$ and (88b) by $\boldsymbol{H}_n$ then adding these we deduce

$$\nabla \cdot (\boldsymbol{E}_n \times \boldsymbol{H}_m^\dagger + \boldsymbol{E}_m^\dagger \times \boldsymbol{H}_n) = 0. \tag{89}$$

Next we separate the transverse $\perp$ and longitudinal $\parallel$ (along the cylinder axes) components according to

$$\boldsymbol{E}_n = \boldsymbol{E}_{n\perp} + \boldsymbol{E}_{n\parallel}, \quad \boldsymbol{H}_n = \boldsymbol{H}_{n\perp} + \boldsymbol{H}_{n\parallel}, \quad \nabla = \nabla_\perp + \boldsymbol{e}_z \frac{\partial}{\partial z}. \tag{90}$$

After the substitution of (90) into (89) we obtain

$$\begin{aligned} &\boldsymbol{e}_z \cdot \frac{\partial}{\partial z} \left[\boldsymbol{E}_{n\perp} \times \boldsymbol{H}_{m\perp}^\dagger + \boldsymbol{E}_{m\perp}^\dagger \times \boldsymbol{H}_{n\perp} \right] \\ &= \nabla_\perp \cdot \Big[\boldsymbol{E}_{n\perp} \times \boldsymbol{H}_{m\parallel}^\dagger + \boldsymbol{E}_{n\parallel} \times \boldsymbol{H}_{m\perp}^\dagger \\ &\qquad + \boldsymbol{E}_{m\perp}^\dagger \times \boldsymbol{H}_{n\parallel} + \boldsymbol{E}_{m\parallel}^\dagger \times \boldsymbol{H}_{n\perp} \Big]. \end{aligned} \tag{91}$$

Taking into account the z-dependence on the modes given by the factors $\exp(i\zeta_n z)$, $\exp(-i\zeta_m^\dagger z)$ and integrating (91) over the unit cell we derive

$$i(\zeta_n - \zeta_m^\dagger) \int_\Omega \boldsymbol{e}_z \cdot (\boldsymbol{E}_{n\perp} \times \boldsymbol{H}_{m\perp}^\dagger + \boldsymbol{E}_{m\perp}^\dagger \times \boldsymbol{H}_{n\perp}) dA = 0, \tag{92}$$

since the integral on the left hand side vanishes due to quasi-periodicity. We finally obtain

$$\int_\Omega \boldsymbol{e}_z \cdot (\boldsymbol{E}_{n\perp} \times \boldsymbol{H}_{m\perp}^\dagger + \boldsymbol{E}_{m\perp}^\dagger \times \boldsymbol{H}_{n\perp}) dA = 0, \tag{93}$$

which holds for arbitrary modes such that $\zeta_n \neq \zeta_m^\dagger$.

The same relation holds for the counter propagating mode m

$$i(\zeta_n + \zeta_m^\dagger) \int_\Omega \boldsymbol{e}_z \cdot (\boldsymbol{E}_{n\perp}^- \times \boldsymbol{H}_{n\perp}^\dagger + \boldsymbol{E}_{m\perp}^\dagger \times \boldsymbol{H}_{n\perp}^-) dA = 0. \tag{94}$$

The minus sign in the superscript position indicates the direction of the propagation. Taking into account the relations $\boldsymbol{E}^{-}_{n\perp} = \boldsymbol{E}_{n\perp}$ and $\boldsymbol{H}^{-}_{n\perp} = -\boldsymbol{H}_{n\perp}$ we can rewrite (94) in the form

$$\int_{\Omega} \boldsymbol{e}_z \cdot (\boldsymbol{E}_{n\perp} \times \boldsymbol{H}^{\dagger}_{m\perp} - \boldsymbol{E}^{\dagger}_{m\perp} \times \boldsymbol{H}_{n\perp}) dA = 0. \tag{95}$$

After subtraction of relation (95) from (94) the orthogonality relation takes form

$$\int_{\Omega} \boldsymbol{e}_z \cdot (\boldsymbol{E}^{\dagger}_{m\perp} \times \boldsymbol{H}_{n\perp}) dA = 0, \tag{96}$$

which states that two distinct modes propagating in the same direction are orthogonal. It is then clear that these modes can always be normalized such that

$$\int_{\Omega} (\boldsymbol{e}_z \times \boldsymbol{H}_{n\perp}) \cdot \boldsymbol{E}^{\dagger}_{m\perp} dA = \delta_{mn}. \tag{97}$$

B. Modal Completeness

From the field expansions we can derive the condition of the modal completeness. The plane waves can be expanded in the following forms:

$$\overline{\boldsymbol{R}}^{E/M}_{s} = \sum_{n} c^{E/M}_{n} (\boldsymbol{e}_z \times \boldsymbol{H}^{\dagger}_{n\perp}), \tag{98}$$

$$\boldsymbol{R}^{E/M}_{s} = \sum_{n} d^{E/M}_{n} \boldsymbol{E}_{n\perp}. \tag{99}$$

By projecting Eq. (98) on the modes $\boldsymbol{E}_{m\perp}$ and using the biorthogonality relations Eq. (97) we deduce (see Eq. (65))

$$c^{E/M}_{m} = \int_{\Omega} \boldsymbol{E}_{m\perp} \cdot \overline{\boldsymbol{R}}^{E/M}_{s} \, dA = J^{E/M}_{sm} \, . \tag{100}$$

Similarly we project (99) onto the adjoint magnetic mode $(\boldsymbol{e}_z \times \boldsymbol{H}^{\dagger}_{m\perp})$ and deduce

$$d^{E/M}_{m} = \int_{\Omega} (\boldsymbol{e}_z \times \boldsymbol{H}^{\dagger}_{m\perp}) \cdot \boldsymbol{R}^{E/M}_{s} \, dA = K^{E/M}_{ms} \, . \tag{101}$$

Thus,

$$\overline{\boldsymbol{R}}^{E/M}_{s} = \sum_{n} K^{E/M}_{ns} (\boldsymbol{e}_z \times \boldsymbol{H}^{\dagger}_{n\perp}), \tag{102}$$

$$\boldsymbol{R}^{E/M}_{s} = \sum_{n} J^{E/M}_{ns} \boldsymbol{E}_{n\perp}. \tag{103}$$

Next we project (99) onto plane wave basis by multiplying both sides of (99) by $\overline{\boldsymbol{R}}^{E/M}_{s'}$ and integrating over the unit cell. We obtain

$$\begin{aligned} \int_{\Omega} \boldsymbol{R}^{E/M}_{s} \cdot \overline{\boldsymbol{R}}^{E/M}_{s'} \, dA &= \sum_{n} K^{E/M}_{ns'} \int_{\Omega} \boldsymbol{E}_{n\perp} \cdot \overline{\boldsymbol{R}}^{E/M}_{s'} \, dA \\ &= \sum_{n} K^{E/M}_{ns'} J^{E/M}_{s'n} = \delta_{ss'}. \end{aligned} \tag{104}$$

The equation (104) represents the completeness relation for the modes. If we introduce the vectors of matrices

$$\boldsymbol{J} = \begin{bmatrix} \boldsymbol{J}^E \\ \boldsymbol{J}^M \end{bmatrix} \text{ and } \boldsymbol{K} = \begin{bmatrix} \boldsymbol{K}^E \\ \boldsymbol{K}^M \end{bmatrix}, \tag{105}$$

where

$$\boldsymbol{J}^{E/M} = \left[J^{E/M}_{sm}\right] \text{ and } \boldsymbol{K}^{E/M} = \left[K^{E/M}_{sn}\right] \tag{106}$$

then the completeness relation Eq. (104) can be written in the matrix form

$$\boldsymbol{J}\boldsymbol{K} \;=\; \boldsymbol{I}, \tag{107}$$

where $\boldsymbol{I}$ is the identity matrix.

The completeness relation of the Rayleigh modes can be established in a similar way. The transverse component of electric and magnetic modal fields can be represented as a series in terms of Rayleigh modes in the region above the grid as

$$\boldsymbol{E}_{m\perp} \;=\; \sum_s \left(J^E_{sm}\boldsymbol{R}^E_s + J^M_{sm}\boldsymbol{R}^M_s\right), \tag{108}$$

$$\boldsymbol{e}_z \times \boldsymbol{H}^{\dagger}_{n\perp} \;=\; \sum_s \left(K^E_{ns}\overline{\boldsymbol{R}}^E_s + K^M_{ns}\overline{\boldsymbol{R}}^M_s\right). \tag{109}$$

By multiplying (108) on (109) and integrating we deduce

$$\begin{aligned} \int_\Omega \boldsymbol{E}^{\dagger}_{m\perp} \cdot (\boldsymbol{e}_z \times \boldsymbol{H}_{n\perp})\, dA \;&=\; \sum_s \left(J^E_{sm}\, K^E_{sn} + J^M_{sm}\, K^M_{sn}\right) \\ &=\; \delta_{nm}. \end{aligned} \tag{110}$$

The completeness relation Eq. (110) can be written in matrix form

$$\boldsymbol{K}\boldsymbol{J} = \boldsymbol{I}. \tag{111}$$

C. Interface and slab Energy conservation and reciprocity relations

Here we briefly outline the derivation of energy conservation relations for the situation when there is no absorption. The flux conservation leads to the certain relations between the Fresnel interface reflection and transmission matrices.

For some value z we can write an expansion

$$\boldsymbol{E}_\perp = \sum_n (c^-_n + c^+_n)\boldsymbol{E}_{n\perp} \tag{112}$$

and similarly

$$\boldsymbol{e}_z \times \boldsymbol{H}_\perp = \sum_n (c^-_n - c^+_n)\boldsymbol{e}_z \times \boldsymbol{H}_{n\perp} \tag{113}$$

The downward flux is defined by

$$S_z = \mathrm{Re}\left[\int \mathrm{E}_\perp \cdot (\mathrm{e_z} \times \overline{\mathrm{H}}_\perp)\right] = \tag{114}$$
$$\frac{1}{2}\left[(\boldsymbol{c}^- - \boldsymbol{c}^+)^H \boldsymbol{U}(\boldsymbol{c}^- + c^+) + (\boldsymbol{c}^- + \boldsymbol{c}^+)^H \boldsymbol{U}^H(\boldsymbol{c}^- - c^+)\right],$$

where the matrix $\boldsymbol{U}$ is given by

$$U_{mn} = \int_\Omega \boldsymbol{E}_{m\perp} \cdot (\boldsymbol{e}_z \times \overline{\boldsymbol{H}}_{n\perp}) dA. \tag{115}$$

The relation (114) can be written in the form

$$S_z = \mathrm{Re}\left\{[\mathrm{c}^{-\mathrm{H}}\, \mathrm{c}^{+\mathrm{H}}]\mathrm{V}\begin{bmatrix} \boldsymbol{c}^- \\ \boldsymbol{c}^+ \end{bmatrix}\right\}, \tag{116}$$

where matrix

$$\boldsymbol{V} = \begin{bmatrix} \frac{1}{2}(\boldsymbol{U} + \boldsymbol{U}^H) & \frac{1}{2}(\boldsymbol{U} - \boldsymbol{U}^H) \\ -\frac{1}{2}(\boldsymbol{U} - \boldsymbol{U}^H) & -\frac{1}{2}(\boldsymbol{U} + \boldsymbol{U}^H) \end{bmatrix} \tag{117}$$

is Hermitian, i.e. $\boldsymbol{V}^H = \boldsymbol{V}$. This is a general result which is applicable also in the presence of absorption. The $\boldsymbol{U}$ matrix is a dense matrix in the presence of absorption. In the absence of absorption it reduces to the following structural form

$$\boldsymbol{U} = \begin{bmatrix} 1 & 0 & 0 & 0 & 0 & 0 & 0 & 0 & \dots & 0 \\ 0 & 1 & 0 & 0 & 0 & 0 & 0 & 0 & \dots & 0 \\ 0 & 0 & 1 & 0 & 0 & 0 & 0 & 0 & \dots & 0 \\ 0 & 0 & 0 & \pm 1 & 0 & 0 & 0 & 0 & \dots & 0 \\ 0 & 0 & 0 & 0 & \pm 1 & 0 & 0 & 0 & \dots & 0 \\ 0 & 0 & 0 & 0 & 0 & \pm 1 & 0 & 0 & \dots & 0 \\ 0 & 0 & 0 & 0 & 0 & 0 & 0 & 1 & \dots & 0 \\ 0 & 0 & 0 & 0 & 0 & 0 & -1 & 0 & \dots & 0 \\ \vdots & & & & & & & & \dots & \vdots \\ 0 & \dots & & & & & & & 0 & 1 \\ \vdots & \dots & & & & & & & -1 & 0 \end{bmatrix}, \tag{118}$$

as we show in Appendix D. Here we have ordered first the propagating modes with real values of ζ_n, then evanescent modes with pure imaginary propagating constants $\zeta_n = \pm i|\zeta_n|$ and finally the evanescent modes with complex valued propagating constants $\zeta_n = \zeta_n' + i\zeta_n''$.

Given the form of the $\boldsymbol{U}$ matrix Eq. (118) the expression for the flux Eq. (116) can be expressed as

$$S_z = [\boldsymbol{c}^- \, \boldsymbol{c}^+]^H \begin{bmatrix} \boldsymbol{I}_m & i\boldsymbol{I}_{\overline{m}} \\ -i\boldsymbol{I}_{\overline{m}} & -\boldsymbol{I}_m \end{bmatrix} \begin{bmatrix} \boldsymbol{c}^- \\ \boldsymbol{c}^+ \end{bmatrix}, \tag{119}$$

where $\boldsymbol{I}_m = \boldsymbol{U}_s$ - a diagonal matrix with unity on the propagating part of the diagonal of $\boldsymbol{U}$, while $\boldsymbol{I}_{\overline{m}} = \boldsymbol{U}_a$ corresponds to the evanescent part of $\boldsymbol{U}$ [see Eq. (119)].

We next develop the energy conservation relations by considering the integration of fields at the interface between free space and the semi-infinite photonic crystal. We write

$$\boldsymbol{c}^- = \boldsymbol{T}_{12}\boldsymbol{f}^- + \boldsymbol{R}_{21}\boldsymbol{c}^+, \tag{120}$$

$$\boldsymbol{f}^+ = \boldsymbol{R}_{12}\boldsymbol{f}^- + \boldsymbol{T}_{21}\boldsymbol{c}^+, \tag{121}$$

while

$$\begin{bmatrix} \boldsymbol{c}^- \\ \boldsymbol{c}^+ \end{bmatrix} = \begin{bmatrix} \boldsymbol{T}_{12} & \boldsymbol{R}_{21} \\ 0 & \boldsymbol{I} \end{bmatrix} \begin{bmatrix} \boldsymbol{f}^- \\ \boldsymbol{c}^+ \end{bmatrix}. \tag{122}$$

We also can rewrite the relation (121) in the matrix form

$$\begin{bmatrix} \boldsymbol{f}^- \\ \boldsymbol{f}^+ \end{bmatrix} = \begin{bmatrix} \boldsymbol{I} & 0 \\ \boldsymbol{R}_{12} & \boldsymbol{T}_{21} \end{bmatrix} \begin{bmatrix} \boldsymbol{f}^- \\ \boldsymbol{c}^+ \end{bmatrix}, \tag{123}$$

while the energy flux in the free space as

$$S_z = [\boldsymbol{f}^- \, \boldsymbol{f}^+]^H \begin{bmatrix} \boldsymbol{I}_1 & i\boldsymbol{I}_{\overline{1}} \\ -i\boldsymbol{I}_{\overline{1}} & -\boldsymbol{I}_1 \end{bmatrix} \begin{bmatrix} \boldsymbol{f}^- \\ \boldsymbol{f}^+ \end{bmatrix}. \tag{124}$$

Now we substitute the relation for modal vector coefficients $\boldsymbol{c}^{\pm}$ Eq. (122) into Eq. (119) and the plane wave coefficients Eq. (123) into Eq. (124) then by equating the total fluxes in free space Eq. (124) and in the photonic crystal Eq. (122) we can write

$$\begin{bmatrix} \boldsymbol{I} & \boldsymbol{R}_{12}^{\mathrm{H}} \\ \boldsymbol{0} & \boldsymbol{T}_{21}^{\mathrm{H}} \end{bmatrix} \begin{bmatrix} \boldsymbol{I}_1 & -i\boldsymbol{I}_{\overline{1}} \\ i\boldsymbol{I}_{\overline{1}} & -\boldsymbol{I}_1 \end{bmatrix} \begin{bmatrix} \boldsymbol{I} & \boldsymbol{0} \\ \boldsymbol{R}_{12} & \boldsymbol{T}_{21} \end{bmatrix} = \begin{bmatrix} \boldsymbol{T}_{12}^{\mathrm{H}} & \boldsymbol{0} \\ \boldsymbol{R}_{21}^{\mathrm{H}} & \boldsymbol{I} \end{bmatrix} \begin{bmatrix} \boldsymbol{I}_2 & -i\boldsymbol{I}_{\overline{2}} \\ i\boldsymbol{I}_{\overline{2}} & -\boldsymbol{I}_2 \end{bmatrix} \begin{bmatrix} \boldsymbol{T}_{12} & \boldsymbol{R}_{21} \\ \boldsymbol{0} & \boldsymbol{I} \end{bmatrix}. \tag{125}$$

where $\boldsymbol{I}_2 = \boldsymbol{I}_m$ and $\boldsymbol{I}_{\overline{2}} = \boldsymbol{I}_{\overline{m}}$ and $\boldsymbol{I}_1$ as defined for the plane waves in Section 2.D.. Expanding these and equating the formed partitions yields four conservation relations

$$\boldsymbol{R}_{12}^{\mathrm{H}}\boldsymbol{I}_1\boldsymbol{R}_{12} + \boldsymbol{T}_{12}^{\mathrm{H}}\boldsymbol{I}_2\boldsymbol{T}_{12} = \boldsymbol{I}_1 + i\boldsymbol{R}_{12}^{\mathrm{H}}\boldsymbol{I}_{\overline{1}} - i\boldsymbol{I}_{\overline{1}}\boldsymbol{R}_{12}, \tag{126}$$

$$\boldsymbol{R}_{12}^{\mathrm{H}}\boldsymbol{I}_1\boldsymbol{T}_{21} + \boldsymbol{T}_{12}^{\mathrm{H}}\boldsymbol{I}_2\boldsymbol{R}_{21} = i\boldsymbol{T}_{12}^{\mathrm{H}}\boldsymbol{I}_{\overline{2}} - i\boldsymbol{I}_{\overline{1}}\boldsymbol{T}_{21}, \tag{127}$$

$$\boldsymbol{R}_{21}^{\mathrm{H}}\boldsymbol{I}_2\boldsymbol{T}_{12} + \boldsymbol{T}_{21}^{\mathrm{H}}\boldsymbol{I}_1\boldsymbol{R}_{12} = i\boldsymbol{T}_{21}^{\mathrm{H}}\boldsymbol{I}_{\overline{1}} - i\boldsymbol{I}_{\overline{2}}\boldsymbol{T}_{12}, \tag{128}$$

$$\boldsymbol{R}_{21}^{\mathrm{H}}\boldsymbol{I}_2\boldsymbol{R}_{21} + \boldsymbol{T}_{21}^{\mathrm{H}}\boldsymbol{I}_1\boldsymbol{T}_{21} = \boldsymbol{I}_2 + i\boldsymbol{R}_{21}^{\mathrm{H}}\boldsymbol{I}_{\overline{2}} - i\boldsymbol{I}_{\overline{2}}\boldsymbol{R}_{21}. \tag{129}$$

The slab energy conservation relations can be found in the similar way as for the interface relations as above. Furthermore the expressions of the energy relations are very similar to the interface relations. The only difference is now the transmission $\boldsymbol{T}_{12}$ and the reflection $\boldsymbol{R}_{12}$ matrices in (129) need to be replaced by the slab reflection and transmission matrices.

D. The flux matrix $\boldsymbol{U}$

The adjoint modes are defined by

$$\mathcal{L}^\dagger \boldsymbol{E}_n^\dagger = \zeta_n^{2\dagger} \mathcal{M}^\dagger \boldsymbol{E}_n^\dagger, \tag{130}$$

with anti-quasi-periodicity condition $\boldsymbol{E}^\dagger(\boldsymbol{r}+\boldsymbol{R}_p) = \boldsymbol{E}^\dagger(\boldsymbol{r}) \exp(-i\boldsymbol{k}_0 \cdot \boldsymbol{R}_p)$ When there is no absorption

$$\mathcal{L} \boldsymbol{E}_n^\dagger = \zeta_n^{2\dagger} \mathcal{M} \boldsymbol{E}_n^\dagger \tag{131}$$

given $\mathcal{L}^\dagger = \mathcal{L}$ and $\mathcal{M}^\dagger = \mathcal{M}$ are then self adjoint operators. Note that even though the operators $\mathcal{M}$ and $\mathcal{L}$ are self adjoint (when there is no absorption) the eigenvalue problem Eq. (131) is not Hermitian because the operator $\mathcal{M}^{-1}\mathcal{L}$ is not self adjoint in general. Therefore the eigenvalues can be real representing propagating modes, as well as complex (pure imaginary or complex) representing evanescent modes. Now from Eq. (131) we deduce

$$\mathcal{L} \overline{\boldsymbol{E}_n^\dagger} = \overline{\zeta_n^{2\dagger}} \mathcal{M} \overline{\boldsymbol{E}_n^\dagger}, \tag{132}$$

where overline means complex conjugation. By comparing Eq. (132) and the original eigenvalue equation we deduce

$$\boldsymbol{E}_{n\zeta^2}^\dagger = \overline{\boldsymbol{E}}_{n\overline{\zeta}^2} \tag{133}$$

For the real eigenvalues ζ we choose $\zeta^\dagger = \zeta$ while for complex ζ we must choose $\zeta^\dagger = -\overline{\zeta}$ which will ensure that the downward evanescent propagating field is decaying. Therefore we have

$$\boldsymbol{E}_{n\zeta}^\dagger = \overline{\boldsymbol{E}}_{n\overline{\zeta}} \tag{134}$$

for the propagating field and

$$\boldsymbol{E}_{n\zeta}^\dagger = \overline{\boldsymbol{E}}_{n,-\overline{\zeta}} \tag{135}$$

for the evanescent field. From Maxwell's equations we deduce that

$$\boldsymbol{H}_{\perp n\zeta}^\dagger = -\overline{\boldsymbol{H}}_{\perp n,-\overline{\zeta}}. \tag{136}$$

Thus, the equations (92) and (94) can be rewritten as

$$(\zeta_m - \overline{\zeta}_n) \int_\Omega \boldsymbol{e}_z \cdot (\boldsymbol{E}_{m\perp} \times \overline{\boldsymbol{H}}_{n\perp} + \overline{\boldsymbol{E}}_{n\perp} \times \boldsymbol{H}_{m\perp}) dA = 0, \tag{137}$$

$$(\zeta_m + \overline{\zeta}_n) \int_\Omega \boldsymbol{e}_z \cdot (\boldsymbol{E}_{m\perp} \times \overline{\boldsymbol{H}}_{n\perp} - \overline{\boldsymbol{E}}_{n\perp} \times \boldsymbol{H}_{m\perp}) dA = 0 \tag{138}$$

Therefore when $\zeta_m \neq \pm\overline{\zeta}$, by adding and subtracting the relations (137) and (138) we may deduce

$$\int_\Omega \boldsymbol{e}_z \cdot (\boldsymbol{E}_{m\perp} \times \overline{\boldsymbol{H}}_{n\perp}) dA = \int_\Omega \boldsymbol{e}_z \cdot (\overline{\boldsymbol{E}}_{n\perp} \times \boldsymbol{H}_{m\perp}) dA = 0, \tag{139}$$

which are the U_{mn} elements of the matrix $\boldsymbol{U}$ introduced earlier. From (138) and for $\zeta_m = \overline{\zeta}_n$ and real ζ_n we deduce that the integral

$$\int_\Omega \boldsymbol{e}_z \cdot (\boldsymbol{E}_{n\perp} \times \overline{\boldsymbol{H}}_{n\perp}) dA \tag{140}$$

is real. When ζ_m is pure imaginary and $\zeta_m = \zeta_n = i\zeta$ then from (138) we deduce that

$$\int_\Omega \boldsymbol{e}_z \cdot (\boldsymbol{E}_{n\perp} \times \overline{\boldsymbol{H}}_{n\perp}) dA \tag{141}$$

is pure imaginary.

Now let us consider the case where ζ_n is complex. The $\boldsymbol{U}$ matrix is defined by (115). For modes $\zeta_m = \zeta$ and $\zeta_n = -\overline{\zeta}$ from (115) and (136) we deduce

$$U_{mn} = \int_\Omega \boldsymbol{E}_{\zeta\perp} \cdot (\boldsymbol{e}_z \times \overline{\boldsymbol{H}}_{-\overline{\zeta}\perp}) dA = -\int_\Omega \boldsymbol{E}_{\zeta\perp} \cdot (\boldsymbol{e}_z \times \boldsymbol{H}^\dagger_{\zeta\perp}) dA. \tag{142}$$

By using the orthonormal condition

$$\int_\Omega \boldsymbol{E}_{\zeta\perp} \cdot (\boldsymbol{e}_z \times \boldsymbol{H}^\dagger_{\zeta\perp}) dA = 1 \tag{143}$$

we find $U_{\zeta_m,\zeta_n} = U_{\zeta,-\overline{\zeta}} = -1$.

For the modes $\zeta_m = -\overline{\zeta}$ and $\zeta_n = \zeta$ from (115) we obtain

$$\begin{aligned} U_{mn} &= \int_\Omega \boldsymbol{E}_{-\overline{\zeta}\perp} \cdot (\boldsymbol{e}_z \times \overline{\boldsymbol{H}}_{\zeta\perp}) dA \\ &= \int_\Omega \overline{\boldsymbol{E}^\dagger_{\zeta\perp} \cdot (\boldsymbol{e}_z \times \boldsymbol{H}_{\zeta\perp})} dA = 1. \end{aligned} \tag{144}$$

So the elements $U_{\zeta_m,\zeta_n} = U_{-\overline{\zeta},\zeta,} = 1$. This means that $(\boldsymbol{U} + \boldsymbol{U}^H)/2$ is a diagonal matrix with unit elements on only the corresponding to propagating modal part.

References

1. J. D. Joannopoulos, R. D. Meade, and J. N. Winn, *Photonic Crystals: Molding the Flow of Light* (Princeton University Press, New Jersey, 1995).
2. T. Asano, B.-S. Song, and S. Noda, "Analysis of the experimental Q factors (∼1 million) of photonic crystal nanocavities," Opt. Express **14**, 1996–2002 (2006).
3. T. F. Krauss, "Slow light in photonic crystal waveguides," Journal of Physics D **40**, 2666 (2007).
4. Z. Yu, A. Raman, and S. Fan, "Fundamental limit of light trapping in grating structures," Opt. Express **18**, A366–A380 (2010).
5. E. Yablonovitch, "Statistical ray optics," J. Opt. Soc. Am. **72**, 899–907 (1982).
6. S. Nishimura, N. Abrams, B. A. Lewis, L. I. Halaoui, T. E. Mallouk, K. D. Benkstein, J. van de Lagemaat, and A. J. Frank, "Standing wave enhancement of red absorbance and photocurrent in dye-sensitized titanium dioxide photoelectrodes coupled to photonic crystals," J. Am. Chem. Soc. **125**, 6306–6310 (2003).
7. A. Chutinan and S. John, "Light trapping and absorption optimization in certain thin-film photonic crystal architectures," Phys. Rev. A **78**, 023825 (2008).
8. B. Tian, X. Zheng, T. J. Kempa, Y. Fang, N. Yu, G. Yu, J. Huang, and C. M. Lieber, "Coaxial silicon nanowires as solar cells and nanoelectronic power sources," Nature **449**, 885–889 (2007).
9. C. Lin and M. L. Povinelli, "Optical absorption enhancement in silicon nanowire arrays with a large lattice constant for photovoltaic applications," Opt. Express **17**, 19371–19381 (2009).
10. N. S. Lewis, "Toward cost-effective solar energy use," Science **315**, 798–801 (2007).
11. P. Würfel, *Physics of Solar Cells: From Basic Principles to Advanced Concepts* (Vch Verlagsgesellschaft Mbh, 2009).
12. J. Li, H. Yu, S. M. Wong, X. Li, G. Zhang, P. G.-Q. Lo, and D.-L. Kwong, "Design guidelines of periodic Si nanowire arrays for solar cell application," Appl. Phys. Lett. **95**, 243113 (2009).
13. R. C. McPhedran, D. H. Dawes, L. C. Botten, and N. A. Nicorovici, "On-axis diffraction by perfectly conducting capacitive grids," Journal of Electromagnetic Waves and Applications **10**, 1085–1111(27) (1996).
14. L. C. Botten, R. C. McPhedran, N. A. Nicorovici, and A. B. Movchan, "Off-axis diffraction by perfectly conducting capacitive grids: Modal formulation and verification," Journal of Electromagnetic Waves and Applications **12**, 847–882(36) (1998).
15. P. M. Morse and H. Feshbach, *Methods of Theoretical Physics, Part I* (McGraw-Hill, 1953).

16. J. Blad and A. S. Sudbø, "Evanescent modes in out-of-plane band structure for two-dimensional photonic crystals," Opt. Express **17**, 7170–7185 (2009).
17. D. J. Kan, A. A. Asatryan, C. G. Poulton, and L. C. Botten, "Multipole method for modeling linear defects in photonic woodpiles," J. Opt. Soc. Am. B **27**, 246–258 (2010).
18. L. C. Botten, M. S. Craig, R. C. McPhedran, J. L. Adams, and J. R. Andrewartha, "The finitely conducting lamellar diffraction grating," Opt. Acta **28**, 1087–1102 (1981).
19. L. Vardapetyan and L. Demkowicz, "Full-wave analysis of dielectric waveguides at a given frequency," Math. Comp. **72**, 105–129 (electronic) (2003).
20. K. Dossou and M. Fontaine, "A high order isoparametric finite element method for the computation of waveguide modes," Comput. Methods Appl. Mech. Engrg. **194**, 837–858 (2005).
21. R. B. Lehoucq, D. C. Sorensen, and C. Yang, *ARPACK users' guide* (Society for Industrial and Applied Mathematics (SIAM), Philadelphia, PA, 1998).
22. A. Bossavit, *Computational Electromagnetism: Variational Formulations, Complementarity, Edge Elements* (Academic Press, 1998).
23. D. Boffi, F. Brezzi, L. F. Demkowicz, R. G. Durán, R. S. Falk, and M. Fortin, *Mixed finite elements, compatibility conditions, and applications* (Springer-Verlag, Berlin, 2008).
24. G. W. Hanson and A. B. Yakovlev, *Operator theory for electromagnetics : an introduction* (Springer, 2002).
25. B. C. P. Sturmberg, K. B. Dossou, L. C. Botten, A. A. Asatryan, C. G. Poulton, C. M. de Sterke, and R. C. McPhedran, "Modal analysis of enhanced absorption in silicon nanowire arrays," Opt. Express **19**, A1067–A1081 (2011).
26. M. A. Green and M. J. Keevers, "Optical properties of intrinsic silicon at 300 K," Progress in Photovoltaics: Research and Applications **3**, 189–192 (1995).
27. J. Meixner, "The behavior of electromagnetic fields at edges," IEEE Trans. Antennas Propag. **20**, 442 – 446 (1972).
28. U. Fano, "Effects of configuration interaction on intensities and phase shifts," Phys. Rev. **124**, 1866–1878 (1961).
29. S. Fan and J. D. Joannopoulos, "Analysis of guided resonances in photonic crystal slabs," Phys. Rev. B **65**, 235112 (2002).
30. R. Asadi, M. Malek-Mohammad, and S. Khorasani, "All optical switch based on Fano resonance in metal nanocomposite photonic crystals," Opt. Comm. **284**, 2230–2235 (2011).

List of Figures

1 Geometry of the problem. The dielectric permittivity and the magnetic permeability of the slab can be dispersive and can have absorption. The unit cell of the array (right panel) can have arbitrary number of inclusions with arbitrary shapes. The direction of the plane wave incident from above the structure can be arbitrarily chosen. 32

2 Schematic of the field representation near the top and bottom interfaces. . . 32

3 Dispersion curves (lossless cylinders). The solid red curves represent solutions such that ζ^2 is real. The dashed blue curves represent solutions such that $\mathrm{Im}(\zeta^2)$ is not zero. The complex solutions ζ^2 occur as conjugate pairs and, in order to differentiate the pairs, we use the term $\mathrm{Re}(\zeta^2) + \mathrm{Im}(\zeta^2)$ for the x-axis instead of $\mathrm{Re}(\zeta^2)$. 33

4 Dotted black curve is the absorption spectrum at normal incidence for a dilute SiNW array (silicon fill fraction is approximately 3.1%). For comparison, the absorptance curves of a homogeneous slab of equal thickness (thin blue curve) and of a homogeneous slab comprising equal volume of silicon (thick red curve) are shown. 33

5 The black dotted curve and the red solid curve are the absorption spectrum, at normal incidence, of dilute SiNW arrays consisting respectively of circular cylinders with radius $a = 60\,\mathrm{nm}$ and square cylinders with side length $a\sqrt{\pi}$. The two types of cylinders have the same cross section area and the same height. 34

6 Dilute SiNW array: Contour plot of the absorptance as a function of the wavelength and the cylinder height h. The cylinder radius and the lattice constant are respectively $a = 60\,\mathrm{nm}$ and $d = 600\,\mathrm{nm}$. 34

7 Dilute SiNW array: Convergence as the plane wave truncation number N_{PM} increases for a fixed wavelength $\lambda = 700\,\mathrm{nm}$ and waveguide truncation number $N_{\mathrm{array}} = 150$. The computed absorptance for $N_{\mathrm{PM}} = 10$ and $N_{\mathrm{array}} = 160$ is $A = 0.13940$ and this value is considered as "exact" and used to compute the error curve. 35

8 Dilute SiNW array: Convergence as the array mode truncation number N_{array} increases. The details given in the caption of Fig. 7 also apply here except that the plane wave truncation number is fixed at $N_{\mathrm{PM}} = 10$. Note that $\zeta_{120} = \zeta_{121}$ is a degenerate eigenvalue. The isolated blue dot corresponds to the truncation value $N_{\mathrm{array}} = 120$ where the error is unexpectedly high; thus the truncation $N_{\mathrm{array}} = 121$ is instead used for the error curve. 35

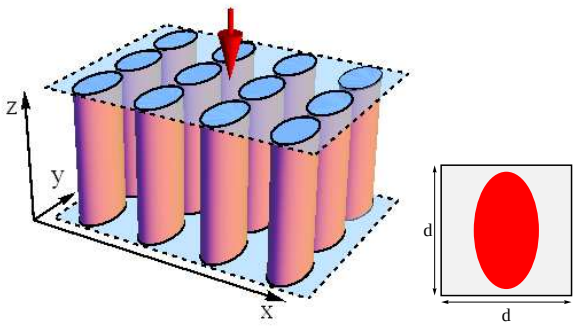

Fig. 1. Geometry of the problem. The dielectric permittivity and the magnetic permeability of the slab can be dispersive and can have absorption. The unit cell of the array (right panel) can have arbitrary number of inclusions with arbitrary shapes. The direction of the plane wave incident from above the structure can be arbitrarily chosen.

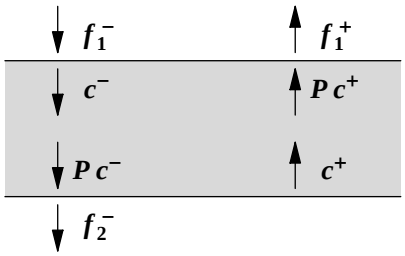

Fig. 2. Schematic of the field representation near the top and bottom interfaces.

9 Off-normal incidence on a dilute SiNW: Absorption spectrum for 45° off-normal orientated along x-axis (azimuthal angle = 0). The solid red and dashed blue curves represent an incidence by TE-polarized and TM-polarized plane wave respectively. The absorption spectrum for normal incidence (Fig. 4) is also shown (dotted black). 36

10 Fano resonances: Transmittance versus normalized frequency for the normal incidence. The radius of the cylinders is $a/d = 0.05$. The resonances in transmission are well resolved. 36

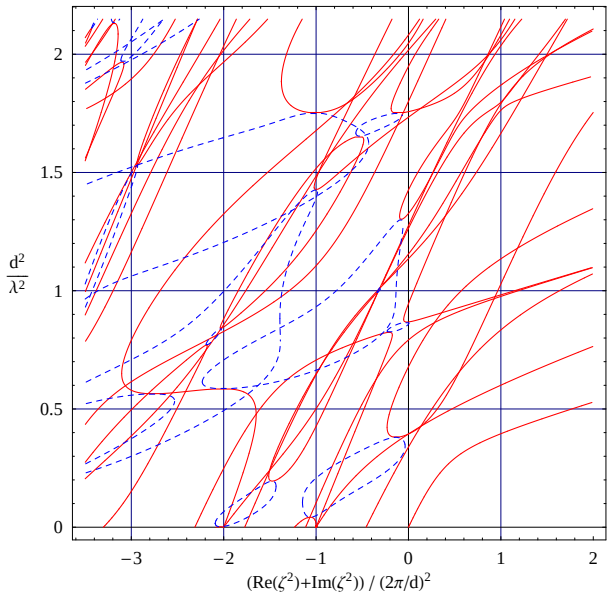

Fig. 3. Dispersion curves (lossless cylinders). The solid red curves represent solutions such that ζ^2 is real. The dashed blue curves represent solutions such that $\mathrm{Im}(\zeta^2)$ is not zero. The complex solutions ζ^2 occur as conjugate pairs and, in order to differentiate the pairs, we use the term $\mathrm{Re}(\zeta^2) + \mathrm{Im}(\zeta^2)$ for the x-axis instead of $\mathrm{Re}(\zeta^2)$.

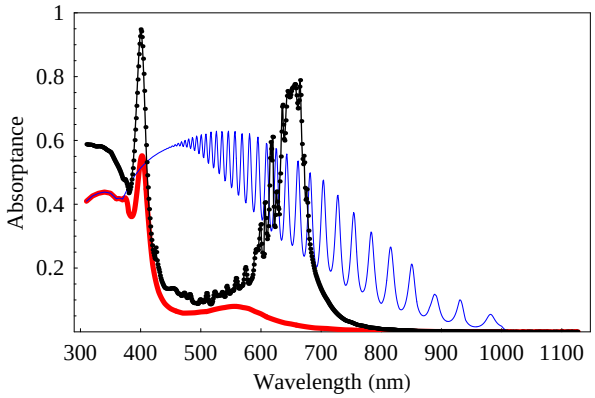

Fig. 4. Dotted black curve is the absorption spectrum at normal incidence for a dilute SiNW array (silicon fill fraction is approximately 3.1%). For comparison, the absorptance curves of a homogeneous slab of equal thickness (thin blue curve) and of a homogeneous slab comprising equal volume of silicon (thick red curve) are shown.

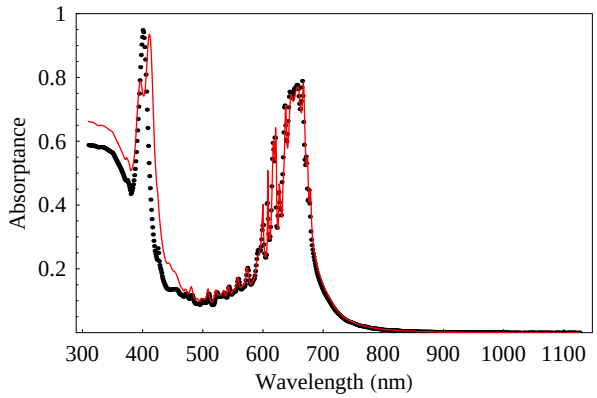

Fig. 5. The black dotted curve and the red solid curve are the absorption spectrum, at normal incidence, of dilute SiNW arrays consisting respectively of circular cylinders with radius $a = 60\,\text{nm}$ and square cylinders with side length $a\sqrt{\pi}$. The two types of cylinders have the same cross section area and the same height.

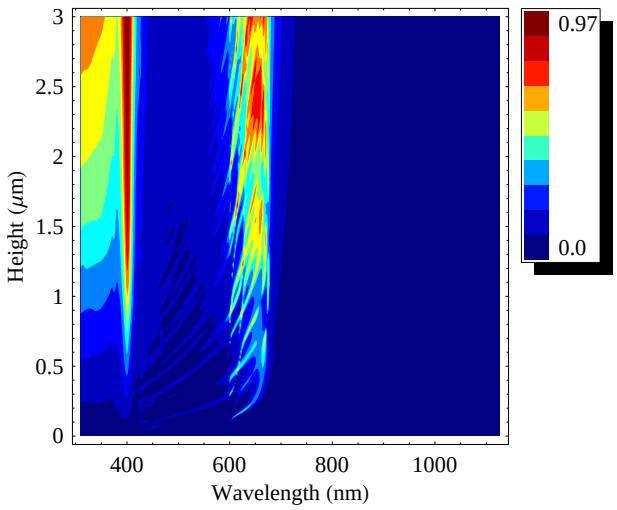

Fig. 6. Dilute SiNW array: Contour plot of the absorptance as a function of the wavelength and the cylinder height h. The cylinder radius and the lattice constant are respectively $a = 60\,\text{nm}$ and $d = 600\,\text{nm}$.

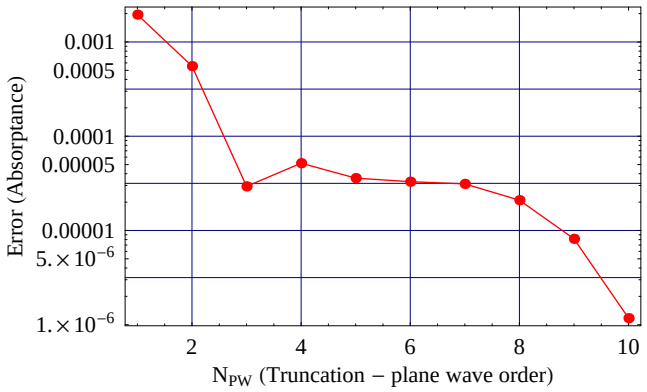

Fig. 7. Dilute SiNW array: Convergence as the plane wave truncation number N_{PM} increases for a fixed wavelength $\lambda = 700\,\mathrm{nm}$ and waveguide truncation number $N_{\mathrm{array}} = 150$. The computed absorptance for $N_{\mathrm{PM}} = 10$ and $N_{\mathrm{array}} = 160$ is $A = 0.13940$ and this value is considered as "exact" and used to compute the error curve.

.

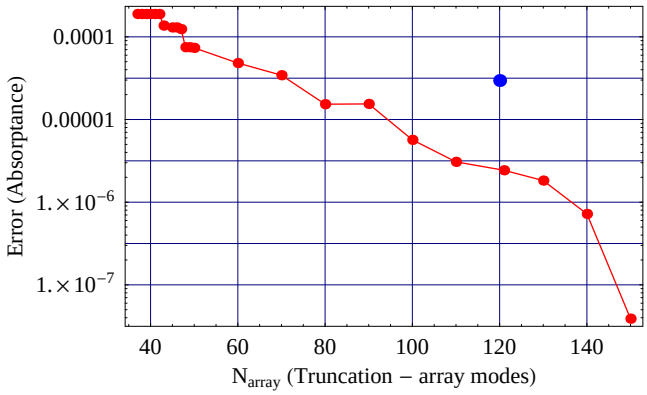

Fig. 8. Dilute SiNW array: Convergence as the array mode truncation number N_{array} increases. The details given in the caption of Fig. 7 also apply here except that the plane wave truncation number is fixed at $N_{\mathrm{PM}} = 10$. Note that $\zeta_{120} = \zeta_{121}$ is a degenerate eigenvalue. The isolated blue dot corresponds to the truncation value $N_{\mathrm{array}} = 120$ where the error is unexpectedly high; thus the truncation $N_{\mathrm{array}} = 121$ is instead used for the error curve.

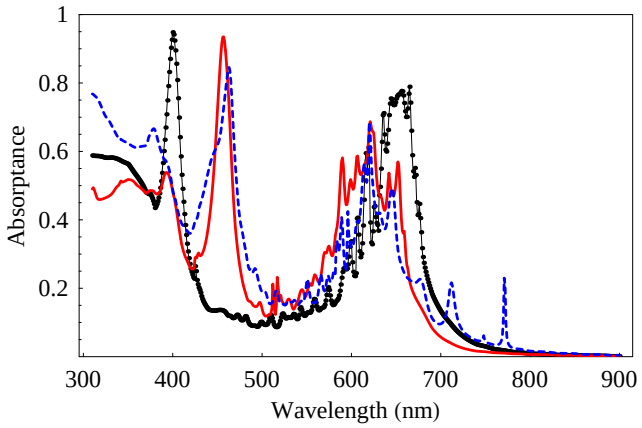

Fig. 9. Off-normal incidence on a dilute SiNW: Absorption spectrum for 45° off-normal orientated along x-axis (azimuthal angle = 0). The solid red and dashed blue curves represent an incidence by TE-polarized and TM-polarized plane wave respectively. The absorption spectrum for normal incidence (Fig. 4) is also shown (dotted black).

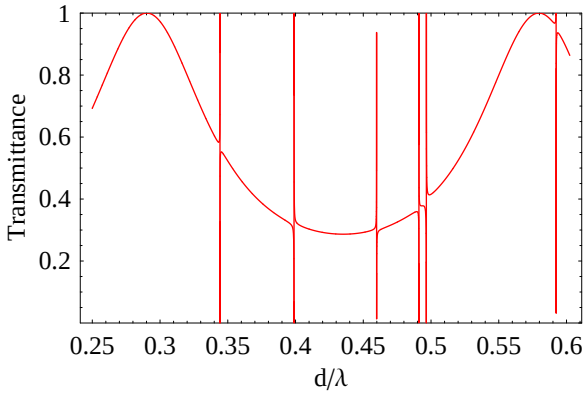

Fig. 10. Fano resonances: Transmittance versus normalized frequency for the normal incidence. The radius of the cylinders is $a/d = 0.05$. The resonances in transmission are well resolved.